Forschungszentrum Karlsruhe
in der Helmholtz-Gemeinschaft
Wissenschaftliche Berichte
FZKA 7245

Experimental Investigations of MHD Flows in a Sudden Expansion

L. Bühler and S. Horanyi

Institut für Kern- und Energietechnik
Programm Kernfusion

August 2006

Forschungszentrum Karlsruhe
in der Helmholtz-Gemeinschaft

Wissenschaftliche Berichte

FZKA 7245

Experimental investigations of MHD flows in a sudden expansion

L. Bühler and S. Horanyi

Institut für Kern- und Energietechnik
Programm Kernfusion

Forschungszentrum Karlsruhe GmbH, Karlsruhe
2006

Forschungszentrum Karlsruhe GmbH
Postfach 3640, 76021 Karlsruhe

Mitglied der Hermann von Helmholtz-Gemeinschaft
Deutscher Forschungszentren (HGF)

ISSN 0947-8620

urn:nbn:de:0005-072457

Experimental investigations of MHD flows in a sudden expansion

Abstract

Reliable theories and models concerning MHD flows in manifolds for fusion applications are important, since most of the pressure drop occurs in those parts of the blanket. Abrupt changes of flow direction in feeding and draining lines as well as expansions and contractions cause flow redistribution and additional pressure drop. Numerical and asymptotic models have been developed during the last years, which require validation on the basis of precise experimental data. Since experimental results available in literature cover only the range of moderate magnetic fields, i.e. $Ha < 300$, and experiments in electrically conducting sudden expansions do not exist, the experimental data base has to be considerably extended in order to cover the fusion relevant range of parameters. For that reason a forced convective MHD experiment in a sudden expansion of rectangular ducts has been designed, manufactured and inserted into the liquid metal NaK-loop of the MEKKA laboratory at the Forschungszentrum Karlsruhe in the frame of the EFDA Technology Work Program TW2-TTBA-006a D1.

Experiments have been performed in which the induced electric potential is measured on the surface of the expanding test section by more than 300 surface potential probes. The pressure variation along the duct has been measured at 16 different axial positions. For high interaction parameters the pressure measurements confirm the theoretical results obtained by an asymptotic theory valid for inertialess flows. Local quantities of the flow, e.g. potential gradients, are inferred with traversable probes at different locations in the ducts. A comparison of experimental and available theoretical results shows quite good agreement and confirms both the validity of the used theoretical tools and the good quality of the measurements. Moreover, due to its valuable contribution to the data base of fundamental MHD flows these experimental results may serve as benchmark basis for future developments of computational MHD tools.

Experimentelle Untersuchungen von MHD Strömungen in plötzlichen Kanalerweiterungen

Zusammenfassung

Zur Vorhersage von MHD Druckverlusten in Strömungsverteilern von Fusionsblankets sind zuverlässige theoretische Analysen und Modelle notwendig, da in diesen Komponenten der Hauptanteil des Gesamtdruckverlusts entsteht. Plötzliche Änderungen der Strömungsrichtung in Zu- und Abfuhrleitungen, sowie in Expansionen und Verengungen, verursachen Strömungsumverteilungen und zusätzlich Druckverluste. In den letzten Jahren wurden asymptotische und numerische Modelle entwickelt, die anhand von experimentellen Daten validiert werden müssen. Da die in der Literatur verfügbaren experimentellen Daten lediglich den Bereich der moderaten Magnetfelder mit Hartmann Zahlen Ha<300 abdecken, und Experimente in elektrisch leitenden, abrupten Expansionen nicht existieren, ist es notwendig, die experimentelle Datenbasis erheblich zu erweitern, um den fusionsrelevanten Parameterbereich abzudecken. Deshalb wurde im Rahmen des EFDA Technologie Programms TW2-TTBA-006a D1 ein Expansionsexperiment entworfen, gefertigt und in den Flüssigmetallkreislauf des MEKKA Labors im Forschungszentrum Karlsruhe eingebaut.

In den Experimenten wurde das induzierte elektrische Potential auf der Oberfläche der Expansionstestrecke an mehr als 300 Messpunkten gemessen. An 16 unterschiedlichen axialen Positionen wurde die Druckverteilung entlang des Kanals bestimmt. Druckmessungen bei großen Interaktionsparametern bestätigen die Vorhersagen einer trägheitsfreien asymptotischen Theorie. Lokale Strömungsgrößen wie z.B. Potentialgradienten wurden mit verfahrbaren Sonden an verschiedenen Positionen in Kanal vermessen. Ein Vergleich der experimentellen und der verfügbaren theoretischen Ergebnisse zeigt gute Übereinstimmung und bestätigt sowohl die Qualität der Theorie als auch der Experimente. Darüber hinaus liefern die hier gewonnenen Ergebnisse einen wichtigen Beitrag zur experimentellen Datenbasis der MHD Grundlagenforschung und können als Benchmark zur Validierung zukünftiger Berechnungsverfahren herangezogen werden.

Experimental investigations of MHD flows in a sudden expansion

Contents

1 Introduction

In the frame work of the European Helium Cooled Lead Lithium (HCLL) blanket for fusion reactors the liquid metal used as breeder material is circulated through the breeder units at very low velocities towards external facilities for tritium extraction and purification of the liquid metal itself. A manifold system distributes the liquid metal into a number of such Breeder units. The connection between the supplying piping system and the breeder units is characterized by extreme contractions and expansions of the cross sections that have been identified as crucial elements. They could create significant pressure drop when the electrically conducting fluid flows through the very high magnetic field confining the plasma.

The current experiment has been designed in order to get insight into the physics involved in MHD expansion and contraction flows. Three dimensional effects will influence the flow and one of the aims of this experiment is to investigate the expanding flows in strong magnetic fields, to get data on pressure distribution along the duct axis by a number of pressure measurements.

Expanding flows in strong magnetic fields undergo severe 3D distortions of the velocity profile which have been investigated through local velocity measurements by electric potential probes both inside the fluid and on the walls. Electric potential can be regarded as a direct measure of the flow in a known magnetic field since it may serve as an approximate hydrodynamic streamfunction of the flow.

At sudden expansions under the influence of strong magnetic fields, like in the present experiment, thin internal layers develop along magnetic field lines. These layers as well as the boundary layers that form along the walls determine essentially the whole flow structure, i.e. velocity and pressure drop.

Expansions and contractions are important elements of actual fusion blankets but they are also basic geometric components of any liquid metal device. They received attention in the past by a number of authors and one should recall as examples the experiments reported by Branover, Vasil'ev and Gel'fgat (1967), Gel'fgat and Kit (1971) who consider inertial MHD flows in insulating sudden expansions for moderate magnetic fields, or Walker, Ludford and Hunt (1972), who study MHD flows through smoothly expanding insulating channels using an inertialess approximation. Smooth expansions with thin conducting walls have been considered by Walker (1981) or by Picologlou, Reed, Hua, Barleon, Kreuzinger and Walker (1989).

In the asymptotic analysis that is often applied to MHD flows in strong magnetic fields, inertia effects are neglected in comparison with the strong Lorentz forces. With this assumption the flow problem becomes linear so that the results obtained for an expansion flow apply as well for a flow in a contraction if the velocity is reversed. This assumption is fairly valid for smooth expansions in strong magnetic fields, when Lorentz forces are much stronger than inertia forces. But we should be aware of the fact that neglecting inertia at sudden expansions requires that the velocities are sufficiently small. Any engineering application in which a fluid is moving, however, has finite values of velocity and of inertia forces even if they may be very small. The present experiment is aimed to study MHD flows at high magnetic fields and to investigate the importance of inertia effects. It is possible to highlight the decreasing influence of inertia forces with increasing magnetic field and to give bounds for the governing parameters beyond which the asymptotic theory is fairly valid.

2 Formulation

The magnetohydrodynamic flow through a sudden expansion of rectangular ducts (see Fig. 1) is governed by nondimensional equations describing the balance of momentum

$$\frac{1}{N}\left[\partial_t \mathbf{v} + (\mathbf{v}\cdot\nabla)\,\mathbf{v}\right] = -\,\nabla p + \frac{1}{Ha^2}\nabla^2\mathbf{v} + \mathbf{j}\times\mathbf{B} \tag{1}$$

and mass conservation

$$\nabla\cdot\mathbf{v} = 0. \tag{2}$$

The electric current density is determined through Ohm's law

$$\mathbf{j} = -\nabla\phi + \mathbf{v}\times\mathbf{B} \tag{3}$$

with equation for charge conservation

$$\nabla\cdot\mathbf{j} = 0. \tag{4}$$

At the fluid wall interface the flow satisfies the no-slip condition

$$\mathbf{v} = 0, \tag{5}$$

the continuity of wall-normal current density

$$\mathbf{j}\cdot\mathbf{n} = \mathbf{j}_w\cdot\mathbf{n} \tag{6}$$

and the continuity of electric potential (no contact resistance)

$$\phi = \phi_w. \tag{7}$$

The last two conditions state that the potential ϕ_w at the wall equals the fluid potential ϕ and the current density in the wall $\mathbf{j}_w$ and in the fluid $\mathbf{j}$ have same normal component. Inside the wall the currents are driven by gradients of the electric wall potential. The duct under investigation is placed in a nonconducting environment (air), so that currents cannot leave the walls through their external surfaces

$$\mathbf{n}\cdot\nabla\phi_w = 0.$$

In the equations shown above $\mathbf{v}$, $\mathbf{B}=\hat{\mathbf{y}}$, $\mathbf{j}$, p, and ϕ stand for velocity, uniform magnetic induction, current density, pressure, and electric potential, scaled by the reference quantities v_0, B_0, $j_0=\sigma v_0 B_0$, $p_0=\sigma v_0 B_0^2 L$, and $\phi_0 = v_0 B_0 L$, respectively. The scale of velocity v_0 is the average velocity in a particular cross section of the duct, and L is a typical length scale. The quantity B_0 is the magnitude of the applied magnetic induction. The fluid properties like the electric conductivity σ, the kinematic viscosity ν, and the density ρ, are assumed to be constant.

The scales used here are standard for MHD flows in strong magnetic fields and they are supported by the present experimental results. With these scales it is possible to

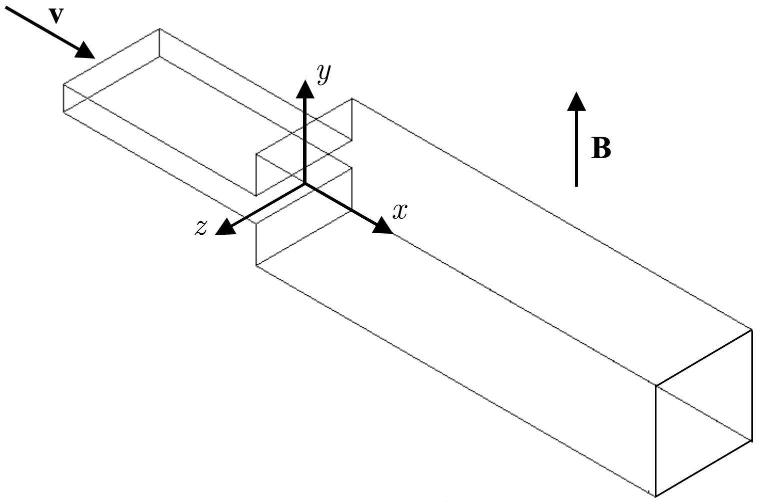

Figure 1: Sketch of expansion geometry showing coordinates and orientation of the magnetic field.

obtain a unique representation of experimental data for different magnetic fields and for velocities that may vary over several orders of magnitude.

The flow is governed by two nondimensional parameters, the Hartmann number Ha and the interaction parameter N

$$Ha = B_0 L \sqrt{\frac{\sigma}{\rho\nu}}\,, \quad N = \frac{\sigma L B_0^2}{\rho v_0}\,. \tag{8}$$

The square of the Hartmann number characterizes the ratio of electromagnetic forces to viscous forces while the interaction parameter represents the ratio of electromagnetic to inertia forces.

The hydrodynamic Reynolds number is related to these quantities via

$$Re = Ha^2/N \tag{9}$$

The conductivity of the walls in comparison with the conductivity of the fluid is expressed through the wall conductance parameter c defined as

$$c = \frac{\sigma_w t_w}{\sigma L}. \tag{10}$$

Here t_w stands for the thickness of the wall and σ_w denotes the electric conductivity of the wall material.

The purpose of the present report is to provide experimental results for liquid-metal MHD expansion flows. Therefore the solution of the equations shown above is not outlined further. Details about solution procedures have been given by Bühler (2003), and Mistrangelo (2005). Nevertheless, the equations are shown here in order to introduce the relevant scaling of the problem, in particular for potential and pressure since results shown below are presented exclusively in those scales.

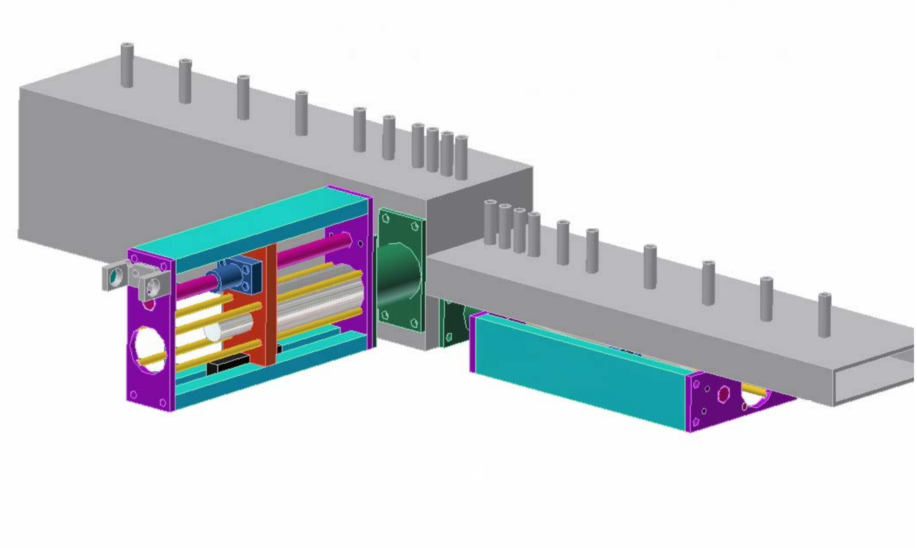

Figure 2: Conceptual design of the expansion test section showing pressure taps at the upper Hartmann walls and mechanical drives for traversable potential gradient probes.

3 The experimental test section

The present experiment considers the flow that expands from a small duct of cross section $2L \times 2L/Z$ into a square duct of size $2L \times 2L$. The expansion ratio is $Z = 4$ and it measures the aspect ratio of large and small ducts, i.e. the ratio of the corresponding Hartmann lengths. In the present example L stands for the half width of both ducts, measured perpendicular to the applied magnetic field. The geometry of the designed experiment as shown in Fig. 2. The typical length scale L has been chosen as large as possible but constrained in such a way that the test section with instrumentation fits into the gap of the magnet. For the experiment we use $L = 0.047\,\mathrm{m}$. The duct walls have a thickness of $t_w = 0.003\,\mathrm{m}$ as a compromise between the both controversial goals of having thin walls with high electric resistance and walls with sufficient mechanical stiffness. The test section has been manufactured from solid pieces of stainless steel by spark erosion in order to avoid welding at the corners. Moreover this procedure yields high precision and sharp internal corners. The test section is composed by several pieces. Some of them are shown in Fig. 3. Three flow straighteners are installed at some distance from both the entrance and the exit of the test section for flow homogenization.

The test section has been manufactured from stainless steel $Mat.no.$1.4571 with electric resistivity $\rho_w = 0.791 \cdot 10^{-6}\,\Omega\,\mathrm{m}$ at 20 °C according to Stahl-Eisen-Werkstoffblätter (1992). This results in a specific electric conductivity of $\sigma_w = 1/\rho_w = 1.264\,2 \cdot 10^6\ 1/\,\Omega\,\mathrm{m}$. Considering the fluid conductivity of NaK at the same temperature, $\sigma = 2.88 \cdot 10^6\ 1/\,\Omega\,\mathrm{m}$ (Jauch, Karcher, Schulz and Haase (1986)) we arrive at a wall conductance parameter of

$$c = \frac{\sigma_w t_w}{\sigma L} = 0.028. \tag{11}$$

The test section has been installed into the liquid metal NaK loop of the MEKKA laboratory (see Sect.4). As a first step, all pressure taps had been closed as shown in Fig.

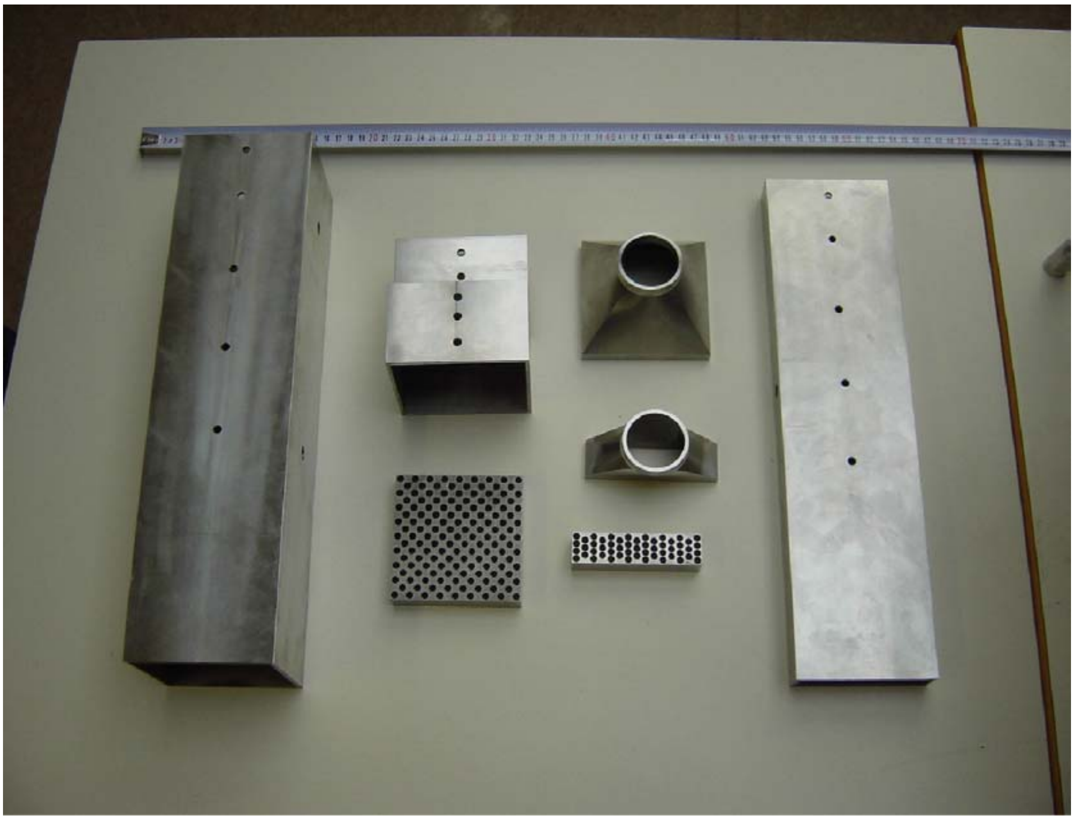

Figure 3: Main parts of the test section before assembling. From left to right: one piece of the large duct, expansion and large flow straightener, fittings for connection with pipes and small flow straightener, one part of the small duct.

Figure 4: Test section during installation into the liquid-metal loop. All pressure taps are closed.

4 and the test section was thermally insulated for the initial wetting runs performed at temperatures above 300 °C. Wetting is an important procedure that has to be performed for each new experimental test section that is inserted into the loop in order to achieve a perfect electrical contact between the fluid and the wall minimizing contact resistance. At those high temperatures the impurities and oxides dissolve into the liquid metal. The wetting campaign was performed over more than a week. Each day, early in the morning, the whole loop was heated up to about 320 °C and kept at this temperature for some hours. In the late afternoon the heating was switched off while the liquid metal was still circulated by the electromagnetic pump at moderate flow rate. Then a certain part of the flow rate was circulated through the cold trap in which dissolved species precipitate on a wire mesh at lower temperature. Practically all the heat of the liquid metal (except some losses through the insulation) was removed by the cold trap. In the late evening, when the loop reached temperatures below 100 °C all systems were switched off. The temperature of the cold trap was chosen to 40 °C initially on the first days and reduced to 30 °C and 20 °C at the last two days. During the entire wetting campaign the loop was kept above 300 °C for more than 35 h.

After all wetting runs were finished, the thermal insulation was removed and the pressure taps were connected to the measuring piping system as shown in Fig. 5. Some pressure taps had to be cleaned because, since these pressure taps act as local cold traps, they were plugged by precipitated impurities. The loop has been pressurized by argon inert gas and a leak detection spray was used to guarantee tightness. All 16 pressure lines were connected to a unipolar pressure-difference measuring system with 5 entrances pipes for the higher pressure level (H) and 14 entrances for the lower ones (L). A remotely controlled valve system connects always one H pipe and one L pipe with a series of four capacitive pressure transducers of different sensitivity. The reading of the most sensitive transducer which has not yet reached saturation is chosen as the pressure value. More details about the pressure measuring system are described in Sect.

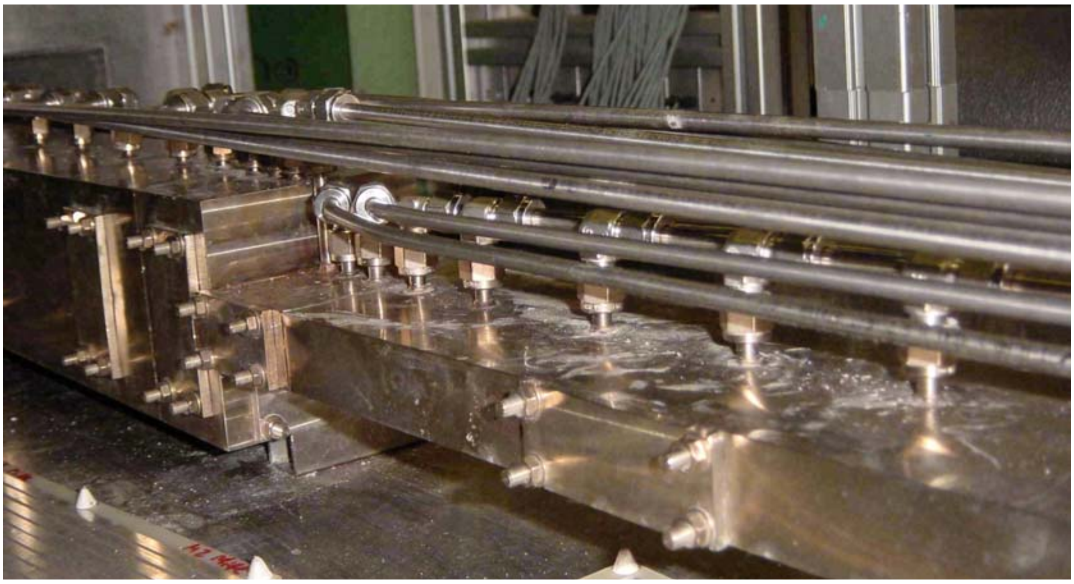

Figure 5: Test section installed in the MEKKA loop. Pressure taps are connected by pipes with the measuring system and covers on the side walls close the openings used for traversable probes.

4.4.

In a second step the test section was covered by insulating plates, which carry more than 300 spring-loaded probes for detecting the electric potential on the duct walls. Since the walls are thin, the potential measured on the outer surface equals approximately the potential at the fluid-wall interface. Potential measurements give essential information on the flow structure in the ducts since potential can be interpreted as an approximate streamfunction for the fluid flow and it can be directly compared with theoretical data. Figure 6 shows the test section with all surface potential probes installed. After all instrumentation is completed the experiment is moved into the magnet.

With the instrumentation described above it was possible to perform all pressure drop - and surface potential measurements. For flows at low velocities, namely below $v_0 = 5\ \mathrm{mm}/\mathrm{s}$, special care had to be taken of the wiring. In particular, signals and grounds had to be arranged in the same cable in order to minimize the noise/signal ratio. For that reason it was necessary in addition to switch the grounds according to the individual signals in parallel with the signal multiplexer.

After these measurements had been completed, traversable probes had been inserted at different axial positions in order to obtain data for local potential, potential gradients, and velocity from the interior of the flow. In the present experiment a four-pole probe was used to measure the local potential and its gradient. This probe was driven through the duct by a traversing mechanism whose mechanical part is shown in Fig. 7. The traversing mechanism was driven through a long rotating axis by a stepping motor located outside the magnetic field. The components of potential gradient $\nabla\phi$ in a plane perpendicular to the applied magnetic field, $\nabla_\perp\phi$, are directly proportional to the two

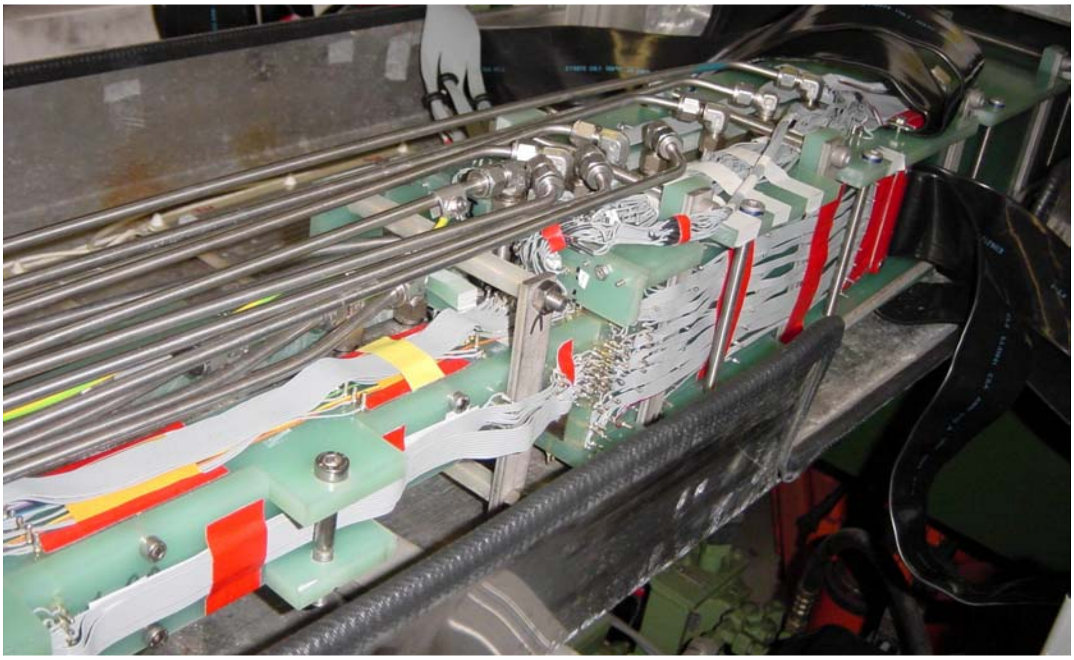

Figure 6: Test section covered with insulating plates that carry more than 300 spring-loaded probes for detection of surface potential. After final instrumentation the whole assembly is moved into the magnet.

components of velocity $\mathbf{v}_\perp$ in the same plane since according to Ohm's law (3)

$$\nabla\phi = \mathbf{v} \times \mathbf{B} \; + ..., \tag{12}$$

where higher order terms (the currents) are usually ignored. This assumption is fairly valid for fully developed flows, when $\mathbf{j} = O(c) \ll 1$, and here we have walls with relatively low conductance ($c = 0.028$). Then we may approximate the velocity in the plane perpendicular to the field as

$$\mathbf{v}_\perp \approx \frac{\partial\phi}{\partial z}\hat{\mathbf{x}} - \frac{\partial\phi}{\partial x}\hat{\mathbf{z}}.$$

For 3D flows the current density may not be as small, so that a direct interpretation of $\nabla\phi$ with $\mathbf{v}_\perp$ is difficult. Nevertheless, the measured $\nabla\phi$ can be compared with $\nabla\phi$ obtained by calculations. With a typical distance l between the sensing tips of the probe of $l = 1.5\,\mathrm{mm}$ and an accuracy of potential difference measurements up to $\pm1\,\mu\mathrm{V}$, it is possible to measure velocities with errors of the order $\Delta v_\perp = \pm\; 0.3 - 1.3\,\mathrm{mm}\,/\,\mathrm{s}$ depending on the strength of the applied magnetic field.

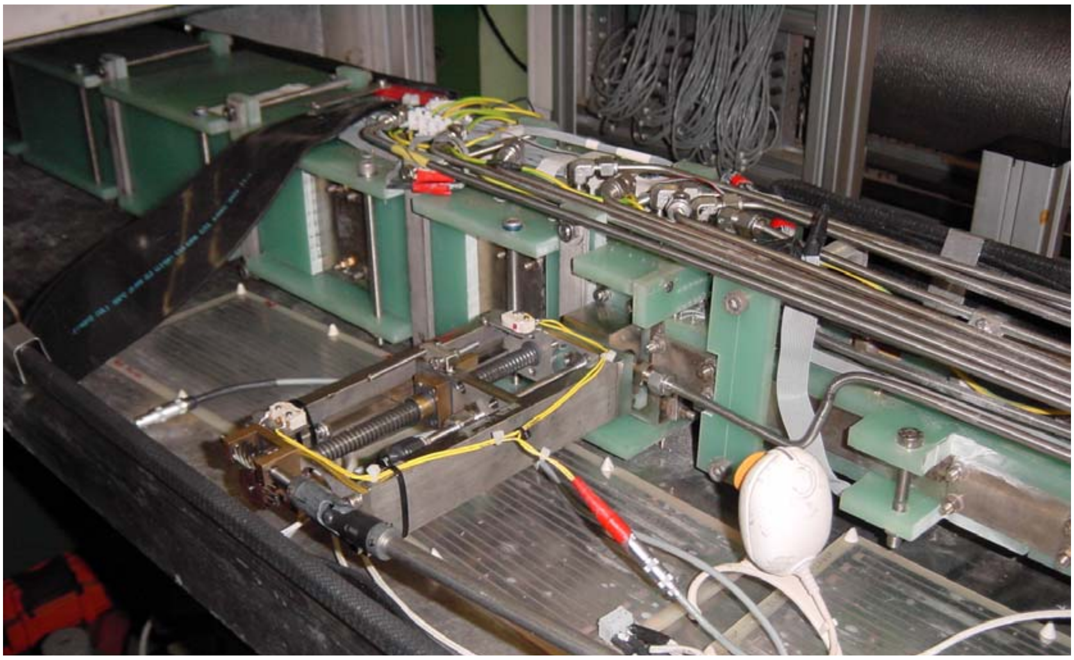

Figure 7: Traversing mechanism for movable potential probes here positioned at the expansion.

4 The MEKKA laboratory

4.1 Liquid metal loop

The present MHD expansion experiment is performed in the MEKKA laboratory of the Forschungszentrum Karlsruhe. The measuring techniques used in the MEKKA-facility have been described previously in a detailed report by Barleon, Mack and Stieglitz (1996). Here we summarize and restrict our description to the most relevant parts. The photograph of MEKKA-facility, in which the expansion test section has been inserted is shown in Fig. 8.

An eutectic sodium-potassium alloy (Na22K78) is used in the liquid metal loop with fluid properties as (Jauch et al. (1986)):

T [°C]	ρ [kg / m^3]	ν [10^{-6} m^2 / s]	σ [10^6 1/ Ω m]
20	868.4	1.05	2.88
40	863.2	0.902	2.79
60	858.1	0.834	2.70

NaK has a lower density and a higher electrical conductivity compared to a lead-lithium alloy Pb-17Li foreseen in the blanket design. This allows in the present experiments to reach, with the available magnet (2 T), high Hartmann numbers up to $Ha = 5800$ which are not too far from fusion applications.

Figure 9 shows a sketch of the liquid metal loop. A canned motor pump with a maximum pressure head of 0.9 MPa at a flow rate of $25\,\mathrm{m}^3/\mathrm{h}$ circulates the liquid metal at temperatures below 250 °C. An additional electromagnetic pump is used for very low flow rates and for high temperature runs. Due to the technical features of the loop and the magnet, the MEKKA facility is capable of attaining interaction parameters in the range of $N = 10^2 - 10^5$, which are appropriate for applications in liquid-metal fusion blankets.

The whole liquid metal loop with pumps, dump volume, expansion tank, heat exchanger, cold trap, pressure transducers, controlling valves etc. is mounted in a rack, which is movable on rails. The arrangement of a movable loop with connected test section enables the operator to place the test section at any desired position relative to the fixed magnet. This allows a good manual access to the instrumented locations of the test section and variable positioning of the experiment within the magnet. Thus, special measurement positions of the test section within the magnetic field can be realized. A hydraulic piston with a stroke of 2500 mm drives the loop including the test section.

The dump volume is fabricated of stainless steel and has a volume of $0.28\,\mathrm{m}^3$. It is filled with $0.2\,\mathrm{m}^3$ of sodium-potassium (NaK). It is foreseen to contain the whole liquid metal volume in non-operation time. Filling of the loop is achieved by first evacuating the whole internal volume from any inert gas. Later a slight argon pressure is applied to the dump volume in order to press the liquid into the loop. After successful filling, pressure equilibration between the top and bottom gas system is established. Draining of the loop after operation and in case of an emergency is performed by gravity.

Accidental liquid metal leaks are detected by short-cut electrodes, which are placed below the rack. In case of a leak the detectors send a signal to a programmable logic controller, which then organizes automatically the shut down of the loop operation and

Figure 8: View on the liquid-metal NaK loop of the MEKKA laboratory

starts the security tasks. In order to ensure a save operation all systems have to be helium leak tight to avoid alkali-oxide reactions.

The purification loop consists mainly of the cold trap with thermostat and electromagnetic flow meters. At high temperatures above 300 °C during the wetting phase a large part of the oxides removed by the NaK from the duct surfaces is dissolved in the liquid metal. In the cold trap the dissolved metal oxides and other impurities are precipitated on a wire mesh and separated from the liquid. The separation process takes advantage of the weaker solubility of the metal oxides in pure NaK at lower temperatures. For this purpose the NaK in the cold trap is cooled by an oil filled thermostat.

The loop with all its systems is totally remote controlled from the operation room. Due to the large amount of components, alarm and level detectors a fully manual operation and a visual control is hardly possible. Moreover, in case of an accident quite a lot of steps have to be made almost simultaneously or in a defined time sequence. All together this would require a large operation team. Therefore, all critical components are connected via alarm sensors to the input gates of a programmable logic controller. Via logic coupling of input signals with output signals the correct control of the components is ensured. Due to the large amount of possible states of the liquid metal loop a number of programs is embedded in the logic controller, which in case of a specific input signal leads to an appropriate reaction. This method is intended to prevent the facility from a maloperation by a user. Two different kinds of programs have to be distinguished: 1.

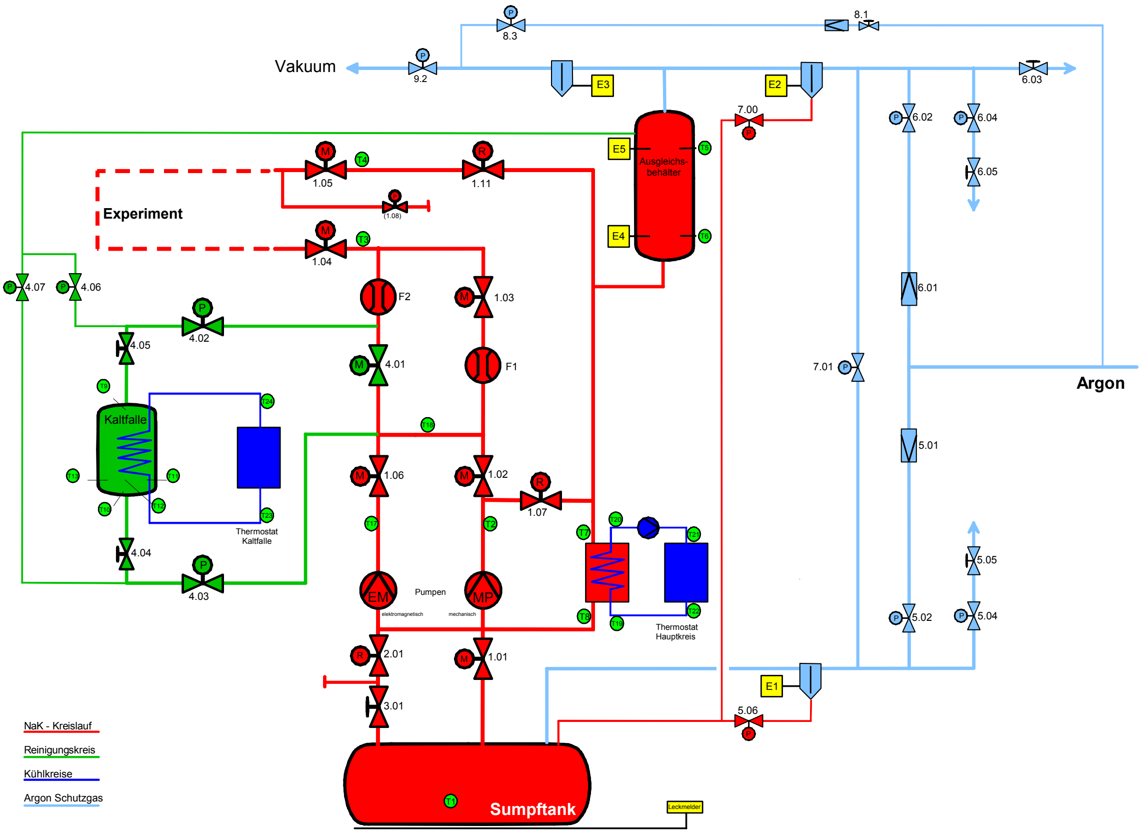

Figure 9: Schematic of the liquid metal NaK loop in the MEKKA laboratory. The different colors indicate different parts of the total system. Red: liquid metal loop; green: purification loop; blue: oil cooling loops (water cooling loops are not shown); light blue: inert gas system.

Operational programs, 2. Security programs. Both types of programs are resident in the logic controller. The operational programs ensure a secure experimental operation, also if alarms of minor importance appear, which would not lead to a damage of the facility. In this case the logic controller shows optically or acoustically the alarm and reacts by its own to the signal. The operational program prevents the user from turning on/off certain components if a signal is present or not, e.g. it is impossible to switch on a fluid pump if the loop is not sufficiently filled.

If critical signals or signal combinations are present at the input of the logic controller, which immediately activates the security programs, which react with a controlled shut down and draining of the loop.

4.2 Magnetic field

The uniform transverse magnetic field is provided for this experiment by a normal conducting dipole magnet. Its maximum field strength is 2.1 T. The magnetic field has a vertical orientation and is directed perpendicular to the axis of the channel. The magnetic gap used for the experiment has a cubic shape and within a region of

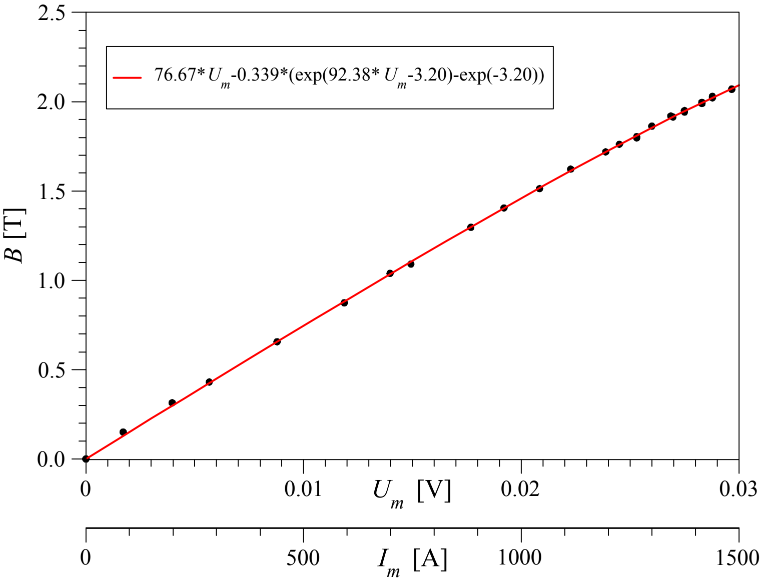

Figure 10: Calibration of magnetic field with measured voltage signal.

800 mm ×480 mm ×165 mm the field is quite uniform with deviations from the core value smaller than 1%. The operation of the magnet requires a variable DC power supply of 300 V and 1500 A. Therefore, a transductor is used, which is three phase fed from the general power supply and which provides $0 - 300$ V at the output. The magnetic field **B** depends approximately linearly on the applied current I_m. However, for higher magnetic fields the magnet feels already weak saturation which is shown by a slightly nonlinear behavior. This slight nonlinearity is taken into account by a calibration fit of measured field intensities as shown in Fig. 10. A measured shunt voltage U_m in a range $0\,\mathrm{V} < U_m < 0.03\,\mathrm{V}$ corresponds to currents I_m in the range between $0\,\mathrm{A} < I_m < 1500\,\mathrm{A}$.

4.3 Flow rate measurements

An important property for the investigation of MHD flows is the total mass flow rate or the volumetric flow rate (mean velocity) that flows through the test section. In order to achieve accurate and redundant results two different types of flow meters are used. One is a so-called gyrostatic (Coriolis) mass flow meter and the other is an electromagnetic flow meter.

The gyrostatic flow meter, as sketched in Fig. 11, measures directly the mass flow rate in the liquid metal loop. The measurement principle is based on the Coriolis force that appears when the fluid moves through the measuring U- tube that is forced to oscillations around the axis A. The Coriolis force tends to tilt the initially horizontal U- loop by a certain angle $\varkappa$ around the axis B. This angle of twist is a direct measure for the mass flow rate $\dot{M}$. Moreover, the eigenfrequency of the U- shaped tube loop depends on the mass that is inside the loop so that the instrument gives additionally information on the density ρ of the fluid. The measurements are independent of the kinematic viscosity and the temperature. The used mass flow meter can be adjusted

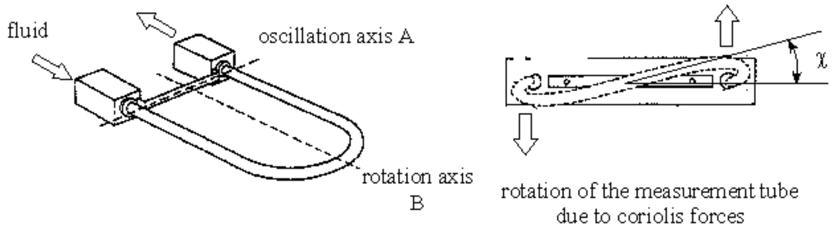

Figure 11: Sketch of the measuring principle of the gyrostatic mass flow meter.

continuously in its measurement range from $\dot{M} = 0 - 3840\,\mathrm{kg}\,/\,\mathrm{h}$ to $0 - 76000\,\mathrm{kg}\,/\,\mathrm{h}$ via remote control. The instrument offers the possibility to a self-calibration if the fluid is at rest. The accuracy of the mass flow meter is quite good with relative errors below 1% of the chosen scale. The operation range of the instrument is limited to temperatures below 200 °C and the maximum pressure limit is 40 bar.

The second type of flow meter is an electromagnetic flow meter. The measurement principle is based on Faraday's law, according to which an electrically conducting medium that moves though a transverse magnetic field experiences an induced electric field. The latter one can be detected by electrodes welded at the sides of a channel or pipe. A photograph of the electromagnetic flow meter used in the MEKKA laboratory is shown in Fig. **??**. The calibration diagram in Fig. 13 shows the almost perfect linearity between mass flux and induced voltage of this instrument in the considered range of flow rates.

Both flow meters were used in parallel in the range of parameters as shown in Fig. 13, i.e. for $\dot{M} = 0 - 10\,000\,\mathrm{kg}\,/\,\mathrm{h}$ $(0 - 2.77\,\mathrm{kg}\,/\,\mathrm{s})$. For higher flow rates it would have been necessary to change the sensitivity of the gyrostatic flow meter which would, however, decrease its accuracy for lower flow rates. For that reason we used explicitly the electromagnetic flow meter for fluxes above $\dot{M} = 2.77\,\mathrm{kg}\,/\,\mathrm{s}$. For smaller flow rates, i.e. for $\dot{M} \lesssim 0.05\,\mathrm{kg}\,/\,\mathrm{s}$ the gyrostatic flow meter in the present scaling starts to loose its accuracy. Moreover, it turned out that also the electromagnetic flow meter shows some nonlinear behavior for small flow rates, which might have its origin in the fact that the flow at the EM-flow meter returns to a laminar state, whereas calibration has been performed in a turbulent regime. A solution to this problem could be achieved by using the first two pressure taps on the test section as an indication for flow rate. Especially for creeping, fully established MHD flows the pressure drop Δp depends linearly on the group $v_0 B^2$. Since pressure drop can be measured with high precision ($\pm 1\,\mathrm{mbar}$), it is possible, after careful calibration, to cover the lower range of flow rates by using the readings of the pressure difference Δp between the first two pressure taps on the experimental test section.

4.4 Pressure difference measurements

The pressure difference measurements are performed in the NaK loop via four capacitive pressure transducers mounted in series. Since the pressure transducers are unipolar, the

Figure 12: Photograph of the electromagnetic flow meter used for the present experiment.

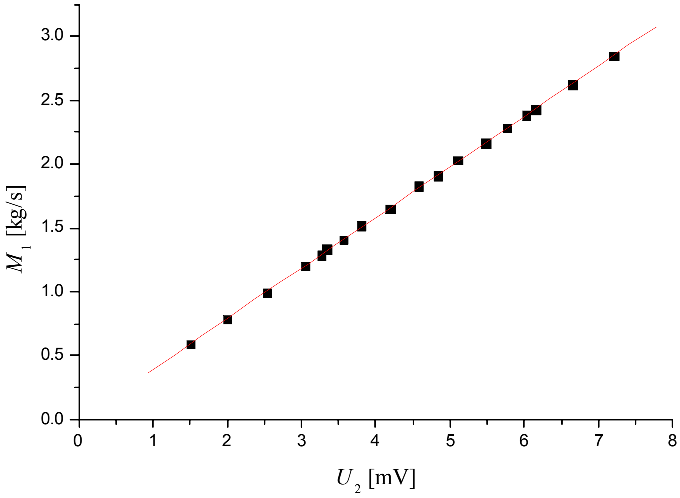

Figure 13: Calibration diagram of the electromagnetic flow meter. Mass flux $\dot{M}_1$ versus induced voltage U_2.

pressure measurement system consists of a line for low pressure, abbreviated with "L" and another one for high pressure, abbreviated with "H", respectively. For details see Fig. 14. All transducers are sensing the same pressure. In order to avoid measurement errors due to nonlinearities near the end of the measurement ranges the ranges for individual transducers are overlapping. From all four readings the one with highest accuracy for the measured data range is selected as *the* measured pressure value.

The measurement principle of a capacitive pressure transducer is very simple. If between the membranes a pressure difference exists the membranes are deformed which leads to a change in electric capacity. This capacity change is transformed in a current $(4\,\mathrm{mA} - 20\,\mathrm{mA})$ that can be measured by a data acquisition system. The accuracy of the pressure transducers used is $\pm 0.5\%$ of the maximum value of the chosen measurement range. An eventual shift of the measurement instrument by temperature changes is compensated by electronics. The operation temperature is limited to 120 °C and the maximum pressure allowed at the membrane is restricted to 140 bar.

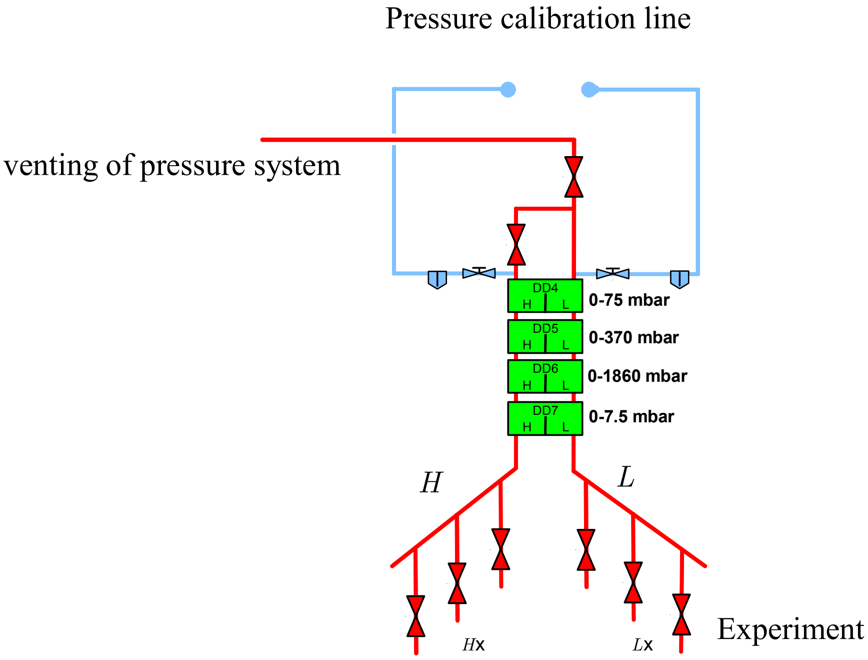

Figure 14: Sketch of the pressure measuring system

4.5 Surface potential measurements

The surface of the test section is covered by insulating plates which carry more than 300 spring-loaded probes for detecting the electric potential on the duct walls. Since the walls are thin, the potential measured on the outer surface equals approximately the potential at the fluid-wall interface. Potential measurements give essential information on the flow structure in the ducts since potential can be often interpreted as an approximate streamfunction for the fluid flow and it can be directly compared with theoretical data. A principle sketch of two spring-loaded needles used for potential measurements is shown in Fig. 15. Some of these needles are displayed in a photograph shown in Fig. 16. The fully instrumented test section with surface potential probes has been already shown in Fig. 6. The cables were connected with a multiplexer that switches packages of 20 signals to a digital multichannel nano-voltmeter, which resolves electric potential differences up to an accuracy of $\pm 0.1\,\mu$V. The multiplexer and the nano-voltmeter were controlled by a computer.

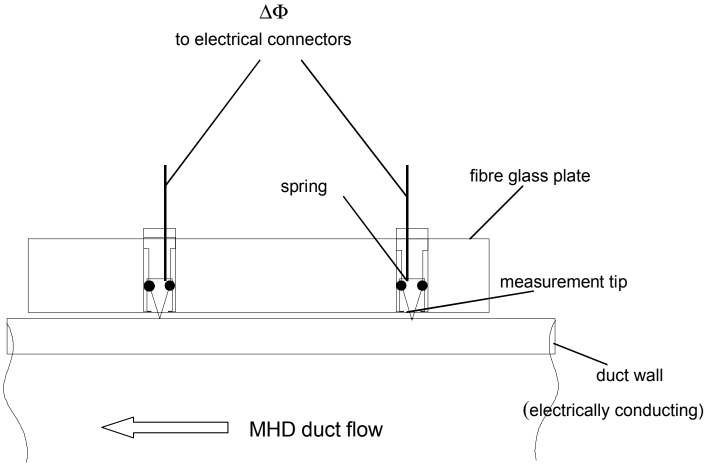

Figure 15: Principle sketch of two spring-loaded needles used for potential difference measurements.

Figure 16: Photograph of an insulating plate showing sensing spring-loaded needles.

In order to get more accurate information about potential distribution at the expansion a non-uniform grid spacing has been used for positioning of the electrodes. A really fine mesh has been used to resolve the expansion region and a coarser one is employed in the upstream and downstream parts. The measuring points are mainly distributed on one half of the duct ($z > 0$) since it has been expected that the potential distribution will be symmetric with respect to the vertical symmetry plane at $z = 0$. Nevertheless,

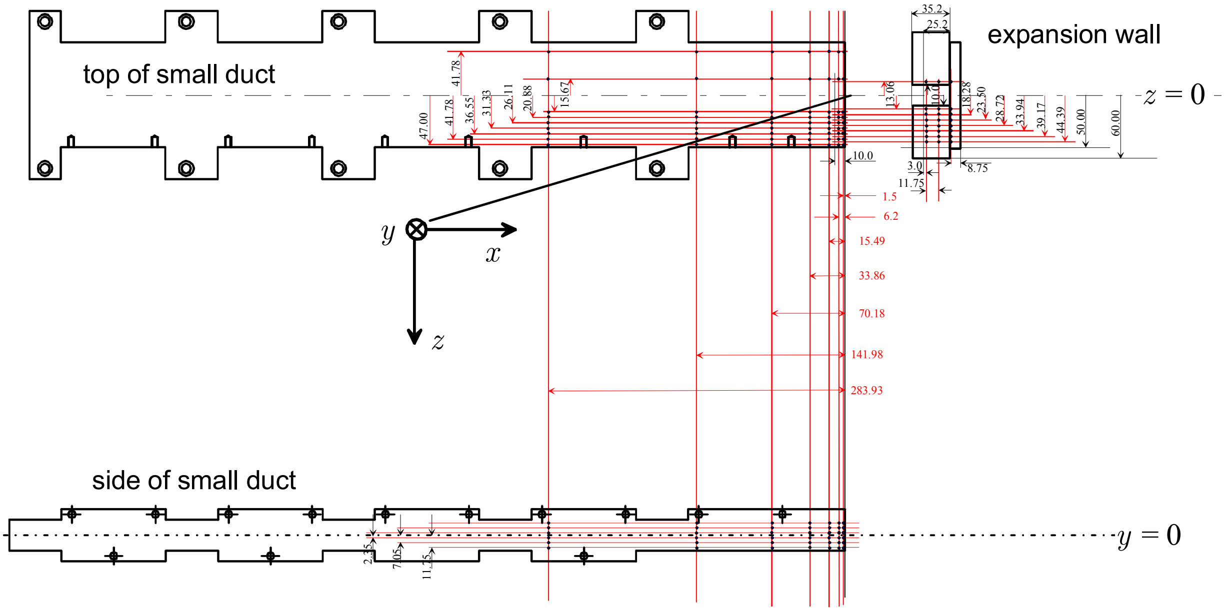

Figure 17: Positions (measured here in mm) of potential probes mounted on the small duct. The figure shows the upper Hartmann wall and the side wall.

for checking symmetry the other half of the upper wall has been equipped with two additional lines of electrodes. In all experiments performed, the symmetry with respect to $z = 0$ could be confirmed. The positions of potential probes on the small and on the large duct are shown in Fig. 17 and in Fig. 18, respectively. These figures display drawings of the insulating plates, mounted around the test section, which carry the potential probes.

4.6 Data acquisition

The measurements were controlled by a computer using a program on the basis of the LabView software. This program controls the valves H_x and L_x of the pressure measuring system, it switches the multiplexer used to measure surface electric potential, it controls and reads the multi-channel nano-voltmeter, the data acquisition cards in the PC etc. Moreover, temperature measurements at the entrance and exit of the test section are used to determine on-line the actual temperature-dependent physical properties of the liquid metal, i.e. $\rho(T)$, $\nu(T)$, $\sigma(T)$, and together with measurements of B and v_0 it is possible to determine immediately the governing nondimensional parameters, the Hartmann number Ha, the interaction parameter N or the Reynolds number Re.

The measurements were arranged in the following way: the magnetic field and the flow rate are adjusted to give desired Hartmann numbers and interaction parameters. The program than switches automatically one of the 16 levels of the multiplexer, where each level switches 20 potential signals to the multi-channel nano-voltmeter. At each multiplexer level the 20 potential signals are scanned by the voltmeter and send to the PC. For each potential signal an integration time of 2 s is used. The total time for potential measurement at one level of the multiplexer is more than enough to reach a

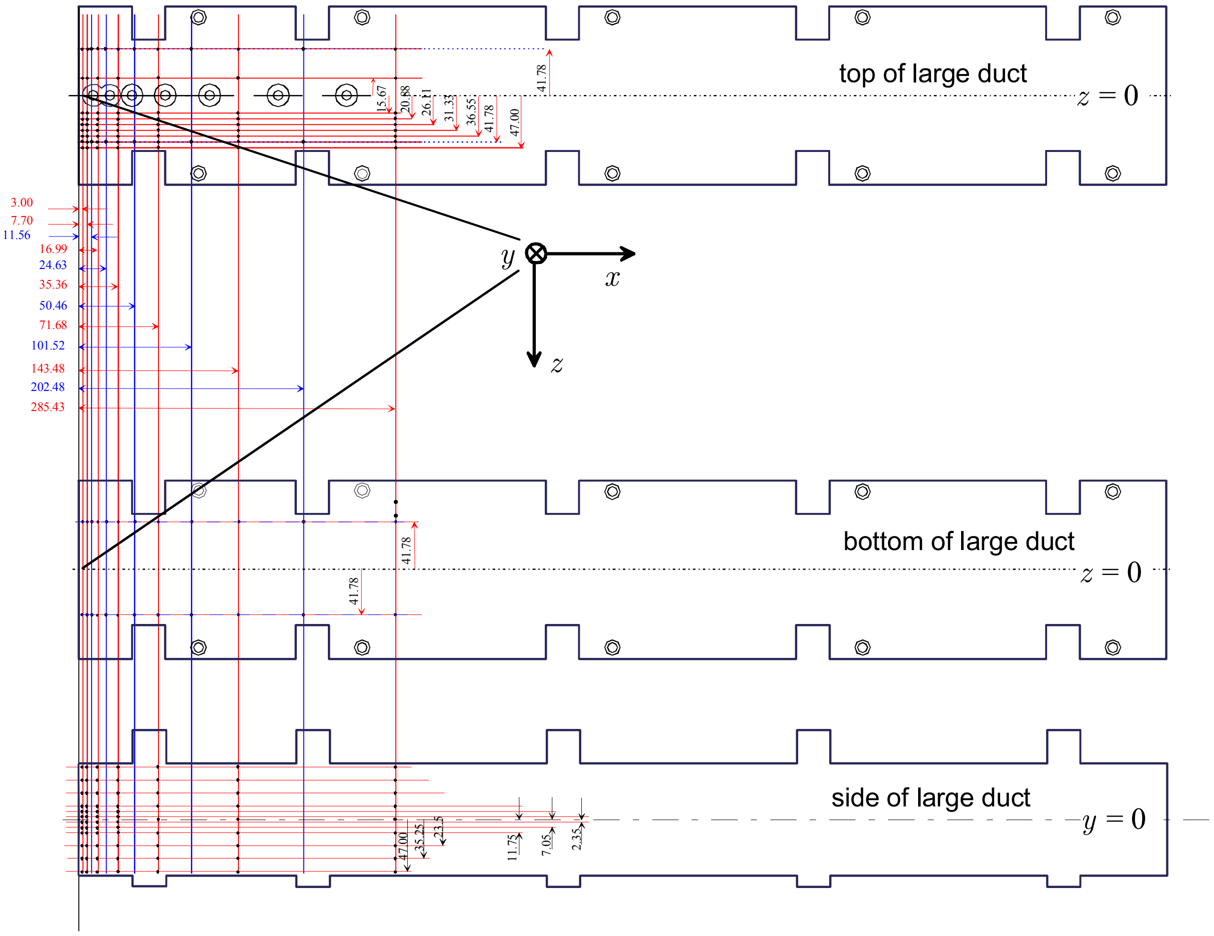

Figure 18: Positions (measured here in mm) of potential probes mounted on the large duct. The figure shows the upper and lower Hartmann walls and the side wall.

steady state reading at the pressure transducer. After the pressure difference is recorded, the multiplexer is switched to the next level, the pressure system is connected to the next pressure taps and the same procedure is repeated. With this program it is possible to record simultaneously surface potential and pressure variations along the duct. Results are plotted online into a diagram for visualization. This is very helpful since irregularities in the data can be detected immediately and inconsistent measurements can be repeated. This is important since during operation it may happen that sometimes a small gas bubble is occasionally trapped in a pressure tap, which leads to wrong pressure data at that line. In all cases when such inconsistencies have been observed, careful venting of the pressure measuring line removed the defect.

5 Results

5.1 Pressure

The pressure has been measured along the upper Hartmann wall at 16 pressure taps for various mean velocities, varying in the large duct in the range $1\,\mathrm{mm}\,/\,\mathrm{s} \lesssim v_0 \lesssim 0.7\,\mathrm{m}\,/\,\mathrm{s}$ and for magnetic fields within $0.18\,\mathrm{T} \lesssim B_0 \lesssim 2\,\mathrm{T}$. As already outlined, all dimensions are scaled with the half width L of the duct and the pressure values shown in the following are scaled with the pressure scale $p_0 = \sigma v_0 B_0^2 L$. All pressure values are shown with respect to the reference pressure at the first pressure tap, i.e. $p\,(x = -6.38) = 0$. The results, shown in Figs.19-23, confirm the validity of the used pressure scaling, since with this scale all results, which were taken in the range between some few mbar and several bar, depending on mean velocity and magnetic field, condense into a unique representation.

The measured data far upstream ($x \ll 0$) and downstream ($x \gg 0$) from the expansion approach perfectly the predicted pressure gradients for fully developed MHD flows in accordance with the asymptotic theory for $N \to \infty$ as indicated by the dashed lines in the diagrams. This shows that the entrance and exit lengths of the experiment are sufficiently long to reach (with the used flow homogenizes at $x \approx \pm 13$) fully established conditions.

The upstream pressure gradient of the fully established flow is considerably higher than that of the downstream flow. This has its origin partly in the fact that the velocity is higher in the small duct. Another reason is that the relative conductance of the wall in comparison with the conductance of the fluid (ratio of wall thickness to local Hartmann length) is higher in the small duct than in the large one. This results in higher currents in the fluid with associated larger pressure drop at upstream positions. The fully established pressure drop in the limit of $Ha \to \infty$ may be estimated according to Bühler (2003) as

$$\frac{\partial p}{\partial x} = -\frac{1}{Y}\frac{\frac{c}{Y}}{1+\frac{c}{Y}+\frac{1}{3}Y}, \tag{13}$$

where c stands for the wall conductance parameter and Y indicates the nondimensional Hartmann length. In the small duct ($x < 0$) we have $Y = 1/Z = 0.25$ and in the large duct ($x > 0$) we have $Y = 1$. This results in limiting values for the nondimensional pressure gradient according to

$$\frac{\partial p}{\partial x} = \left\{ \begin{array}{lcl} -0.37479 & & x < 0 \\ & \text{for} & \\ -0.02057 & & x > 0 \end{array} \right. , \qquad \text{as } Ha \to \infty. \tag{14}$$

This simple design formula aims in giving a first estimation about the order of magnitude of the pressure drops to be expected in the fully developed regions upstream and downstream of the expansion. The finite Hartmann number (viscous effects) present in experiments and applications increases the pressure drop slightly with respect to the above formula. What can be seen here for $c \ll 1$ is that an increase in Hartmann length Y decreases the fully established pressure drop by more than a factor of Y^2.

Near the expansion the pressure drops more rapidly due to three-dimensional recirculating electric currents, associated with additional Joule dissipation. A small fraction

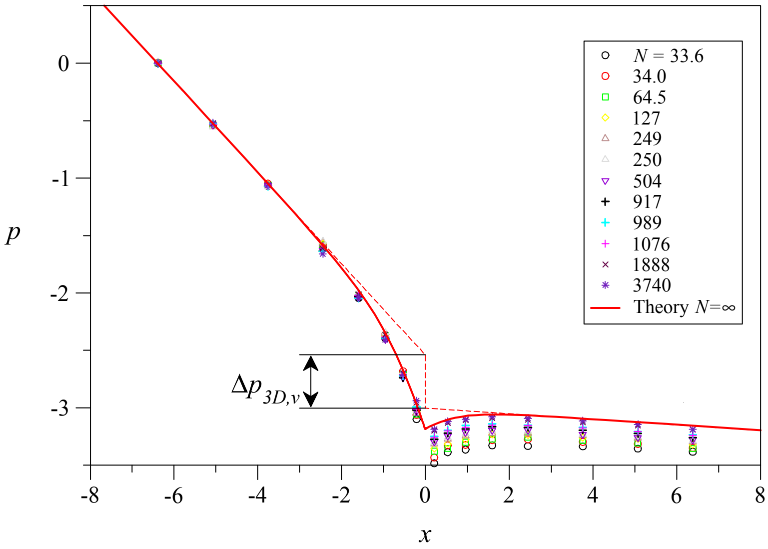

Figure 19: Pressure along the upper Hartmann wall for $Ha = 1000$ and various interaction parameters N.

of this extra pressure drop is recovered behind the expansion in the downstream duct but a major part, called Δp_{3D} remains irreversibly lost.

Results are shown here in Figs.19-23 for Hartmann numbers in the range $1000 \leq Ha \leq 5000$. Each figure displays results for flows at a fixed magnetic field, i.e. for a constant Hartmann number Ha, while the velocity or equivalently the interaction parameter N or the Reynolds number Re have been widely varied by more than two orders of magnitude. All results show that with increasing interaction parameter N, the measured distribution of pressure converges monotonically towards the red solid line that has been obtained by asymptotic-numeric analysis (see e.g. Bühler (2003)). These measurements confirm quite well the accuracy of the computational approach which is valid in the inertialess limit as $N \to \infty$.

As indicated in Figs. 23 the total pressure drop is composed by several different contributions. The two most obvious parts arise from the fully established flows in the small and large ducts, which are well known from literature (Chang and Lundgren (1961), Walker (1981), Bühler (2003)). The fully developed pressure gradients are indicated in the figures by the red dashed lines that extrapolate the entrance and exit conditions towards the position $x = 0$. As mentioned above, near the expansion there appears an additional pressure drop caused by 3D effects due to velocity redistribution and extra current flow. This part Δp_{3D} depends in general on all parameters that govern the flow, namely on the Hartmann number Ha and on the interaction parameter N (or the Reynolds number Re). Results for Δp_{3D} are summarized in Fig. 24. The figure shows experimental data extracted from Figs. 19-23 for finite values of N. The points shown on the vertical axis, i.e. for $N = \infty$ ($N^{-1/3} = 0$) have been obtained by the asymptotic analysis and added to the diagram. They are indicated in Figs. 19-23 as $\Delta p_{3D,v}$. From the figure it is possible to estimate a linear behavior of Δp_{3D} on the quantity $N^{-1/3}$ with increasing slope for higher Hartmann numbers. The slope in the

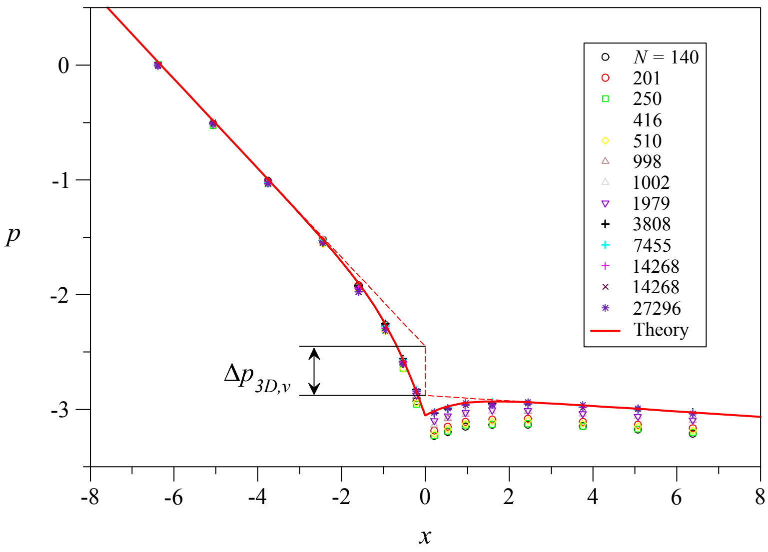

Figure 20: Pressure along the upper Hartmann wall for $Ha = 2000$ and various interaction parameters N.

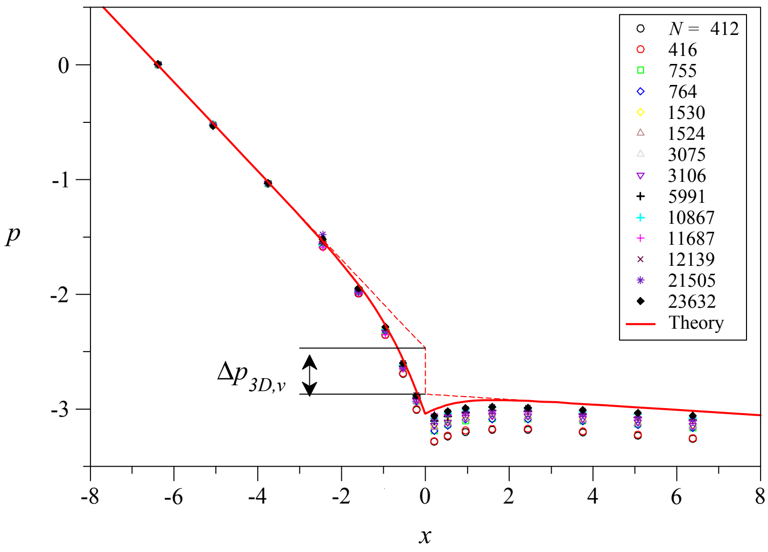

Figure 21: Pressure along the upper Hartmann wall for $Ha = 3000$ and various interaction parameters N.

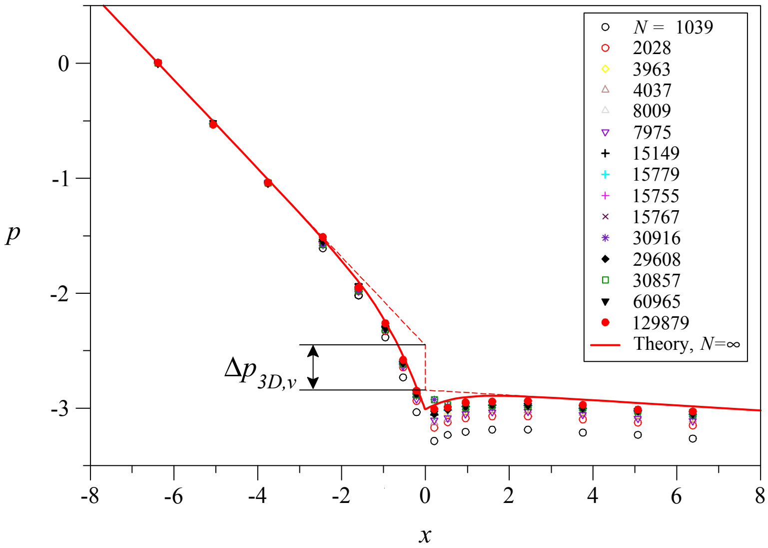

Figure 22: Pressure along the upper Hartmann wall for $Ha = 4000$ and various interaction parameters N.

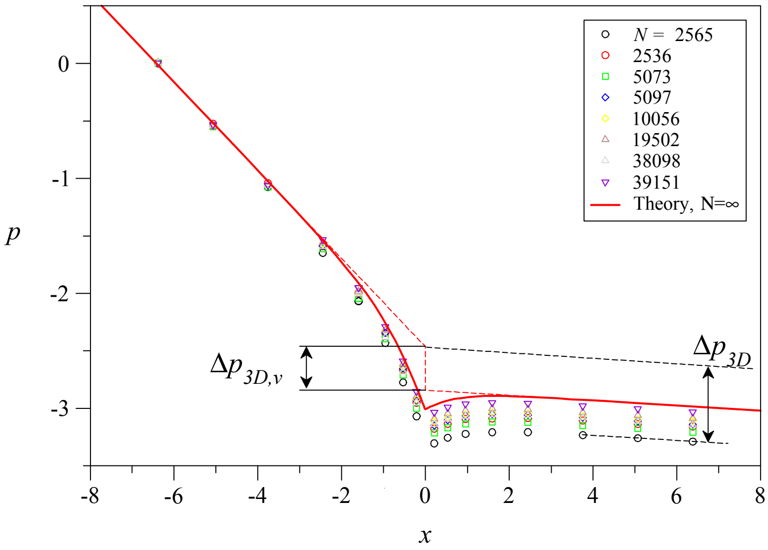

Figure 23: Pressure along the upper Hartmann wall for $Ha = 5000$ and various interaction parameters N.

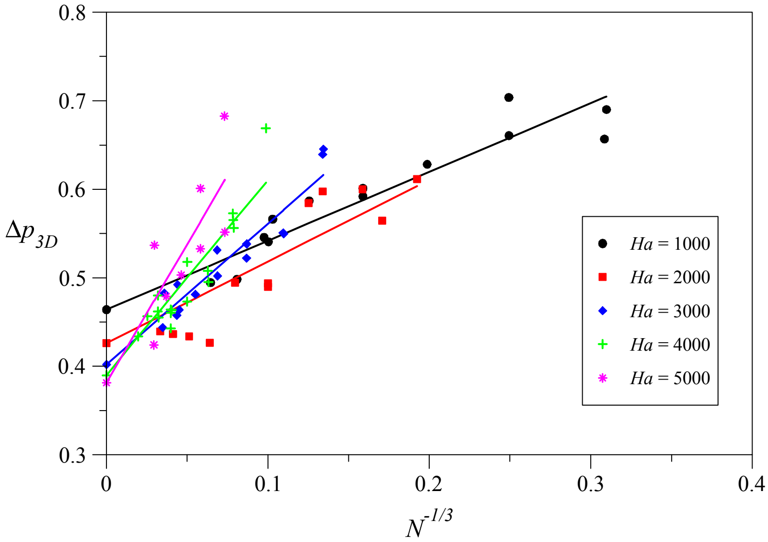

Figure 24: Three-dimensional pressure drop Δp_{3D} as a function of the $N^{-1/3}$.

diagram is obtained as a best fit of the experimental data points.

For further investigation we decompose Δp_{3D} in their inertialess parts $\Delta p_{3D,v}$ shown in Fig. 24 for $N^{-1/3} = 0$, and into inertial parts $\Delta p_{3D,i}$ that are determined by the slopes of the fitted data points. The first part arises for creeping viscous MHD flows and can be described perfectly by the inertialess theory. This fraction of pressure drops has its origin in 3D current loops that close their path both through the conducting walls and through the viscous layers. For that reason $\Delta p_{3D,\nu}$ in creeping MHD flows depends on the interaction of viscous forces and electromagnetic forces, i.e. it depends on the Hartmann number Ha. With increasing Hartmann number the viscous layers become progressively thinner so that their contribution to the current path vanishes as $Ha \to \infty$. A detailed study of this effect is displayed in Fig. 25, which shows clearly the linear dependence of $\Delta p_{3D,\nu}$ on $Ha^{-1/2}$. In the asymptotic limit as $Ha \to \infty$ the 3D pressure drop approaches a value of $\Delta p_{3D,\infty}$, where viscous contributions are not present any more. This value of pressure drop depends exclusively on the geometry of the ducts and scales most sensitively with the expansion ratio Z and with the wall conductance parameter c as shown by Wetzel (2004). For finite values of the Hartmann number a viscous part appears which, depending on the Hartmann number, can reach a similar magnitude as $\Delta p_{3D,\infty}$. From the results shown in Fig. 25 we conclude that for our experiment with $Z = 4$ and $c = 0.028$ the 3D pressure drop of creeping MHD flows scales for high Hartmann numbers as

$$\Delta p_{3D,v} = \Delta p_{3D,\infty} + 4.76\ Ha^{-1/2}, \tag{15}$$

where $\Delta p_{3D,\infty} = 0.315$ stands for the 3D pressure drop for MHD flows at $Ha \to \infty$ and $N \to \infty$, ($Re \to 0$).

A dependence of flow properties on $Ha^{-1/2}$ is typical for flows in which parallel layers are important. The results indicate that the parallel layers in the present experiment play a key role in understanding the physics of the flow at the expansion and for the

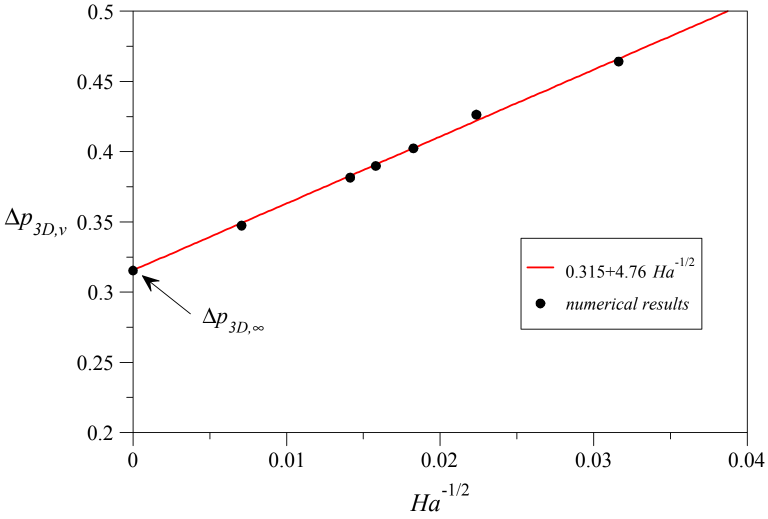

Figure 25: Viscous part of the three-dimensional pressure drop $\Delta p_{3D,v}$ as a function of $Ha^{-1/2}$. $\Delta p_{3D,\infty}$ stands for the 3D pressure drop for MHD flows at $Ha \to \infty$ and $N \to \infty$.

prediction or simulation of abruptly expanding MHD flows. Such parallel layers are present along the side walls of the ducts and their thickness in the inertialess limit is known to scale as $\delta_s \sim Ha^{-1/2}$. In addition, at the expansion, an internal parallel layer develops along the expansion wall and spreads through the fluid along magnetic field lines. This layer, which is called here the expansion layer, is also known from literature as the Ludford layer (Hunt and Leibovich (1967)) and its thickness scales for creeping flows also as $\delta_e \sim Ha^{-1/2}$. For finite values of Ha, 3D current loops find additional paths through these layers, which increases the total current density near the expansion and creates increased pressure drop proportional to these currents. Moreover, these layers are able to carry a significant amount of flow rate in thin, high-velocity jets and they determine by this fact the flow in the whole geometry. The possibility for an intense exchange of flow between cores, expansion layer and side layers has been addressed already by Bühler (2003) or by Mistrangelo (2005). The experimental investigation of this point will be outlined later on in a separate subsection.

In addition to those pressure drop contributions discussed above it is possible to identify another part that has its origin in inertial effects, which become increasingly important for flows at higher velocity, i.e. at higher Reynolds numbers. The total additional 3D pressure drop due to the expansion then is obtained as the sum of the viscous contribution $\Delta p_{3D,v}$ (that contains also the inviscid part $\Delta p_{3D,\infty}$) and the inertial part $\Delta p_{3D,i}$ as

$$\Delta p_{3D} = \Delta p_{3D,v} + \Delta p_{3D,i}. \tag{16}$$

The magnitude of the inertial part $\Delta p_{3D,i}$ depends on the Hartmann number Ha, the Reynolds number Re or the interaction parameter N. From a comparison of the two representations shown in Figs. 26 and 27 one could conclude that the results find a convenient and compact representation as

$$\Delta p_{3D,i} \approx (8.2 \pm 2.2) \cdot 10^{-3}\ Re^{1/3} \tag{17}$$

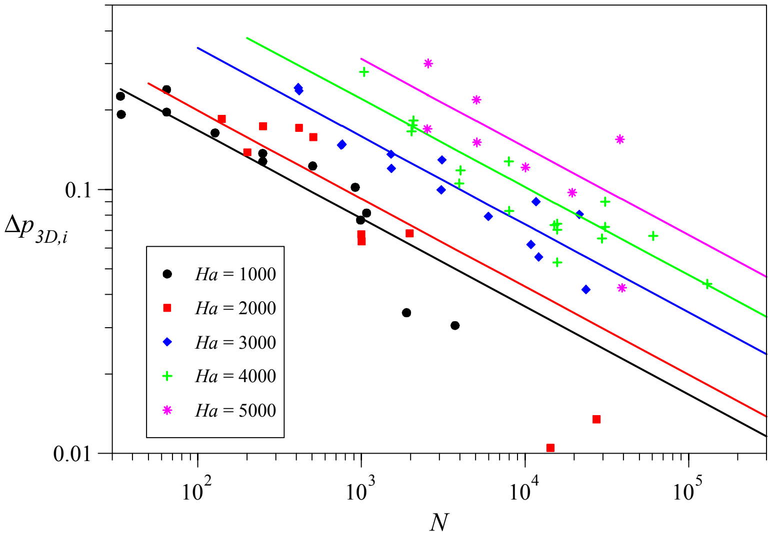

Figure 26: Inertial part of three-dimensional pressure drop, $\Delta p_{3D,i}$, as a function of N.

for all Reynolds numbers and Hartmann numbers that have been investigated. There are, however, some minor exceptions for Hartmann numbers $Ha = 1000$ and 2000, where in the lower range of Reynolds numbers the measured inertial pressure drop was smaller than the value predicted by (17). This could have its origin in the fact that the pressure drops $\Delta p_{3D,i}$ for small Re are at the limit of accuracy of the measuring system. On the other hand the pressure values for small Reynolds numbers and $Ha \leq 2000$ are so small that they do not constitute any problem in engineering applications. The parameter range of higher Reynolds numbers and higher Hartmann numbers that creates significant inertial pressure drop is well represented by the conservative correlation shown above.

Summarizing the discussed results, the correlation that represents at best the measurements according to our knowledge can be written as

$$\Delta p_{3D} = 0.315 + 4.76\ Ha^{-1/2} + (8.2 \pm 2.2) \cdot 10^{-3}\ Re^{1/3}. \tag{18}$$

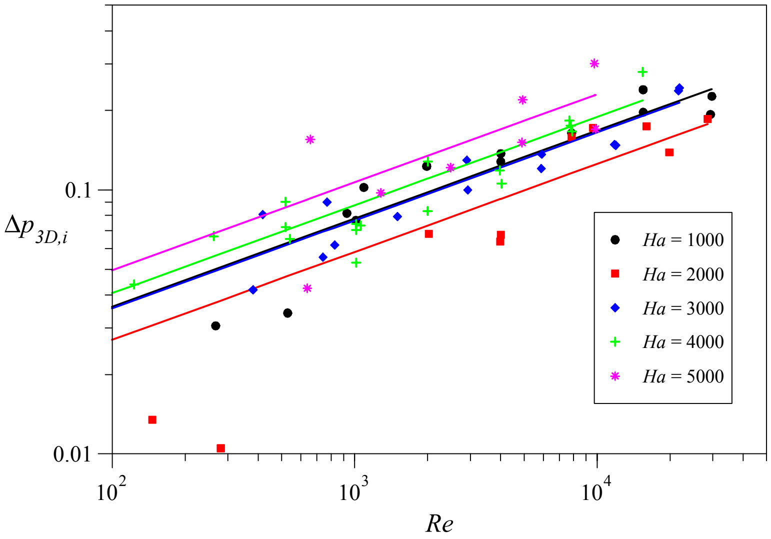

Figure 27: Inertial part of three-dimensional pressure drop, $\Delta p_{3D,i}$, as a function of Re.

5.2 Velocity

Data for local velocity may be extracted from measurements of local potential or to be more precise by the measurement of local potential gradients. For that reason traversable potential probes have been moved through the duct at different axial positions. A sketch of the traversable probe is shown in Fig. 28. The potential gradient may be directly interpreted as a velocity signal since, according to Ohm's law (3), velocity may be derived from

$$-\nabla\phi + \mathbf{v} \times \hat{\mathbf{y}} = \mathbf{j} = 0 + O\left(c\right),$$

which leads to an approximation of axial and transverse velocity components as

$$u \approx \frac{\partial\phi}{\partial z}, \quad w \approx -\frac{\partial\phi}{\partial x}. \tag{19}$$

The potential gradient approximates the velocity usually quite well if current density is small. This is the case e.g. for fully developed flows in ducts with thin walls when $c \ll 1$ or in insulating straight ducts. Near the expansion, where additional 3D currents are present, the velocity according to (19) might require a correction, but still the transverse gradient of potential which has been recorded correctly may serve as validation data for numerical tools.

The probe has been used to measure the absolute value of potential ϕ, i.e. the potential difference between the point **a** and the ground **g** (reference potential, $\phi_{\mathrm{g}} \equiv 0$) that is located on the upper Hartmann wall at the symmetry plane

$$\phi\left(z_{\mathrm{a}}\right) = \phi_{\mathrm{a}} - \phi_{\mathrm{g}}. \tag{20}$$

The horizontal components $\nabla_{\perp}\phi$ of the potential gradient (transverse and axial, in the plane perpendicular to $\mathbf{B}$) are obtained by recording the following three potential differences:

$$\Delta\phi_{\mathrm{ab}} = \phi_{\mathrm{a}} - \phi_{\mathrm{b}}, \quad \Delta\phi_{\mathrm{bc}} = \phi_{\mathrm{b}} - \phi_{\mathrm{c}}, \quad \Delta\phi_{\mathrm{ca}} = \phi_{\mathrm{c}} - \phi_{\mathrm{a}}. \tag{21}$$

For details of the geometry see Fig. 28. The transversal and axial potential gradients are then calculated using the known positions of the sensing tips of the probes located at

$$\mathbf{a} = \left(x_{\mathrm{a}}, 0, z_{\mathrm{a}}\right), \quad \mathbf{b} = \left(x_{\mathrm{b}}, 0, z_{\mathrm{b}}\right), \quad \mathbf{c} = \left(x_{\mathrm{c}}, y_{\mathrm{c}}, z_{\mathrm{c}}\right). \tag{22}$$

The probe was initially designed in such a way that $x_{\mathrm{a}} = x_{\mathrm{b}}$. However, because of difficulties during fabrication both axial positions differ slightly and this small difference is taken into account during evaluation of the data. The electrode at position **c** is located slightly out of the symmetry plane, shifted by the small quantity $y_{\mathrm{c}} \ll 1$. Nevertheless its recorded value can be directly used as the potential value at $y = 0$ since $\phi_{\mathrm{c}} \approx \phi\left(x_{\mathrm{c}}, 0, z_{\mathrm{c}}\right) + \partial\phi/\partial y\left(x_{\mathrm{c}}, 0, z_{\mathrm{c}}\right) y_{\mathrm{c}}$, where the last term vanishes due to symmetry. Although two potential differences were sufficient to determine the horizontal potential gradients we measured all the three, in order to check the quality of the measurements since

$$\Delta\phi_{\mathrm{ab}} + \Delta\phi_{\mathrm{bc}} + \Delta\phi_{\mathrm{ca}} = \varepsilon, \tag{23}$$

where ε should be theoretically zero. For practical measurements we check if ε (in dimensional units) does not exceed values of about $1\,\mu$V. The horizontal potential gradient $\nabla_\perp \phi = \partial_x \phi \, \hat{\mathbf{x}} + \partial_z \phi \, \hat{\mathbf{z}}$ is then obtained from the system of equations

$$\Delta\phi_{\mathrm{ab}} = \nabla_\perp \phi \cdot (\mathbf{a} - \mathbf{b}) = \frac{\partial \phi}{\partial x} (x_{\mathrm{a}} - x_{\mathrm{b}}) + \frac{\partial \phi}{\partial z} (z_{\mathrm{a}} - z_{\mathrm{b}}) , \tag{24}$$

$$\Delta\phi_{\mathrm{ca}} = \nabla_\perp \phi \cdot (\mathbf{c} - \mathbf{a}) = \frac{\partial \phi}{\partial x} (x_{\mathrm{c}} - x_{\mathrm{a}}) + \frac{\partial \phi}{\partial z} (z_{\mathrm{c}} - z_{\mathrm{a}}) , \tag{25}$$

where all horizontal coordinates of the sensing tips are taken into account.

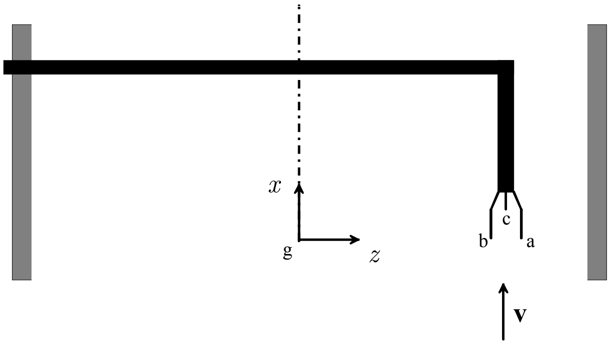

Figure 28: Sketch of traversable potential probe.

5.2.1 Profiles of upstream potential

Let us start the discussion of local flow properties for a cross section located upstream the expansion at $x = -5.6$. The Figs. 29 - 33 display nondimensional values of potential according to eq. (20), recorded for different Hartmann numbers ranging from $Ha = 1000$ up to $Ha = 5000$. For each Hartmann number the flow rate (Reynolds number Re or interaction parameter N) was varied over a wide range. The lower bound of the range of Re was the accuracy of the measuring system (lower limit of v_0, upper limit for N). The upper one was given by the power of the pump and the mechanical strength of the test section (upper limit of v_0, lower limit for N). What is observed here is, as expected for unidirectional MHD flows, a linear variation of potential in the center of the duct, i.e. in the core. This is another indication that fully developed conditions are well established at $x = -5.6$ before the flow approaches the expansion. Deviations from the linear law are present only near the side wall at $z = 1$. Unfortunately there exist no data points in the vicinity of the other side wall near $z = -1$ because it was not possible, for geometrical restrictions of the traversing mechanism, to move the probe closer to this wall.

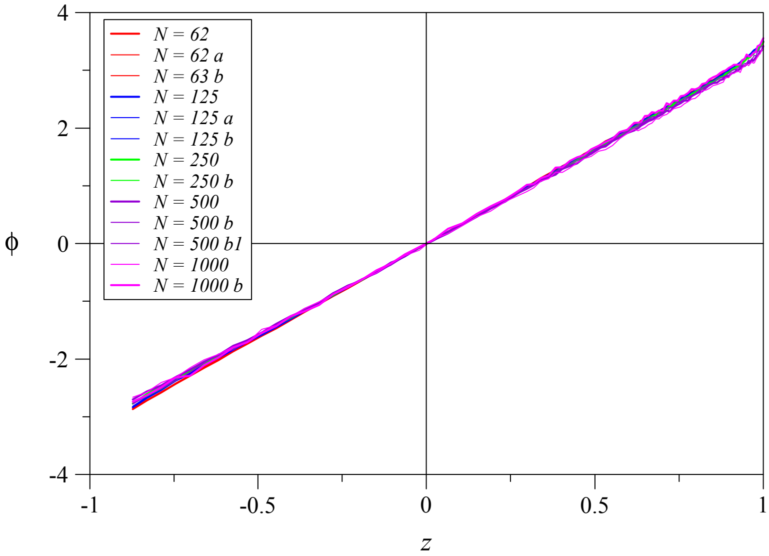

Figure 29: Potential $\phi(z)$ at $x = -5.6$, $y = 0$ for $Ha = 1000$ and different N.

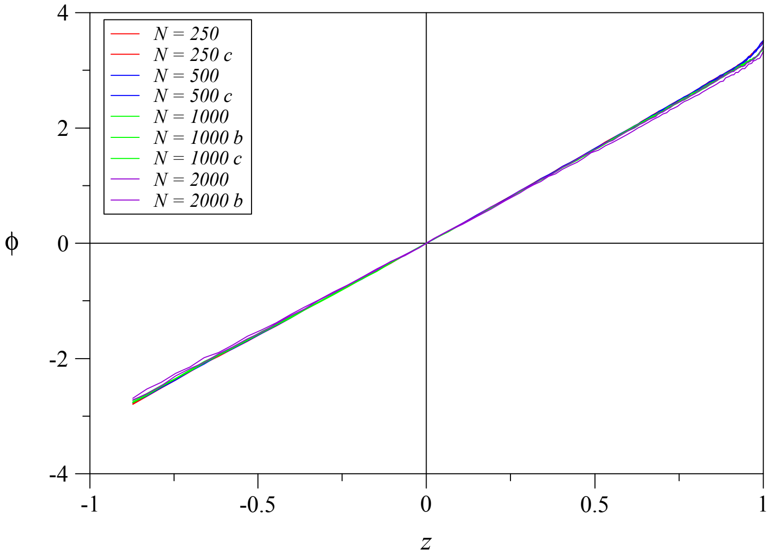

Figure 30: Potential $\phi(z)$ at $x = -5.6$, $y = 0$ for $Ha = 2000$ and different N.

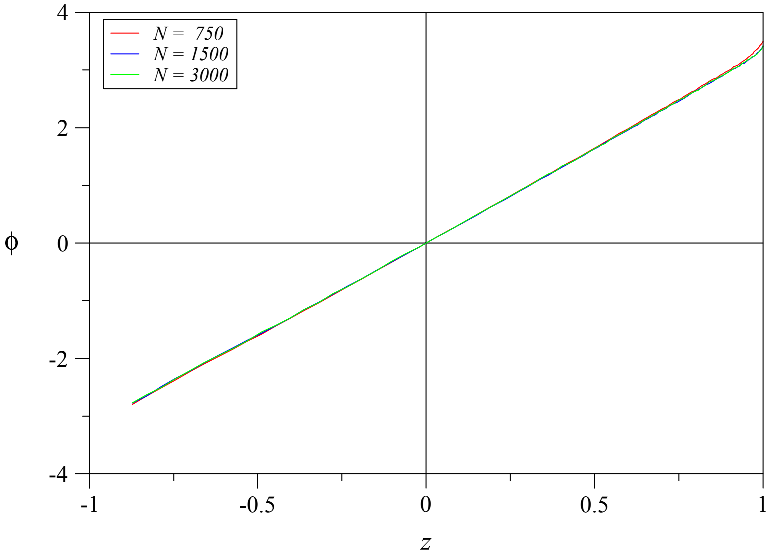

Figure 31: Potential $\phi(z)$ at $x = -5.6$, $y = 0$ for $Ha = 3000$ and different N

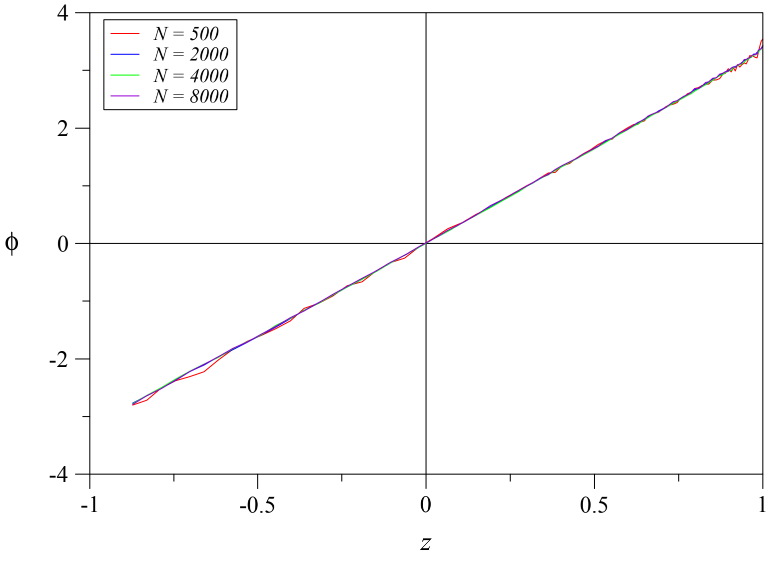

Figure 32: Potential $\phi(z)$ at $x = -5.6$, $y = 0$ for $Ha = 4000$ and different N.

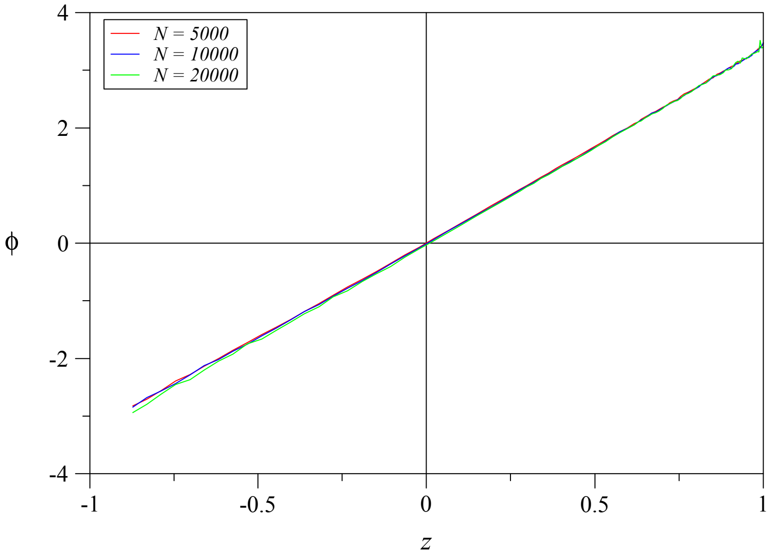

Figure 33: Potential $\phi(z)$ at $x = -5.6$, $y = 0$ for $Ha = 5000$ and different N.

5.2.2 Profiles of upstream axial velocity

After the potential is known, it is straightforward to evaluate the local transverse potential gradient, which approximates the axial velocity in fully developed flows as $u \approx \partial\phi/\partial z$, by differentiation of potential with respect to z. On the other hand it is possible to compare these values with those derived from direct measurements of local potential gradient according to eq. (24) and (25). For higher and moderate velocities both sets of data are in good agreement and confirm thus the quality of the current experiments. For smaller velocities, however, the local potential gradients measured directly by the probe underestimate the real potential gradient as calculated from the absolute value of potential. Therefore those results have been rescaled in order to fit the potential gradient data obtained by differentiation of ϕ. The moderate disagreement is most probably caused by the fact that the probe itself disturbs the local flow field, since especially for high Hartmann numbers, the probe generates a wake type depression of the velocity profile by the formation of internal parallel layers that spread along magnetic field lines from the probe towards the Hartmann walls. Results for various Hartmann numbers and interaction parameters are shown in Figs. 34-38.

This type of internal layers forms not only in the vicinity of the tip of the probe but also along its whole shaft that crosses part of the duct cross section from the side wall $z = -1$ to the tip at $z = z_\mathrm{a}$. For that reason the flow is weakly blocked in $-1 < z \lesssim z_\mathrm{a}$ and as a result increased in $z_\mathrm{a} < z < 1$. This fact explains the slight slope of core velocity. With increasing magnetic field, i.e. for higher Ha, this systematic disturbance of the flow increases.

As a result of all our measurements at the upstream position $x = -5.6$ we observe a flat uniform value of velocity or potential gradient in the core with a strong increase towards the side walls where the high-velocity jets are present. Since these jets are very thin and the probe size is finite, it is not possible for the largest Hartmann numbers under consideration to resolve the region of viscous decay towards the side wall. Nevertheless it is possible to investigate the behavior of the flow near the side wall $z = 1$. In general one can summarize the results as follows: for the highest investigated interaction parameters the side layers are found to be very thin. This is in accordance with the theoretical predictions which suggest that the side layers are as thin as $Ha^{-1/2}$. With increasing Reynolds number (decreasing N) the mean thickness of the side layers becomes suddenly larger. This effect is caused by the occurrence of instabilities of the jet flow along the side walls. The laminar flow becomes unstable, shows time-dependent variations with increased exchange of momentum with the core. As a result, the side layers become thicker on a temporal average. A complete description of this observation is out of the scope of the present report and will be described separately in future.

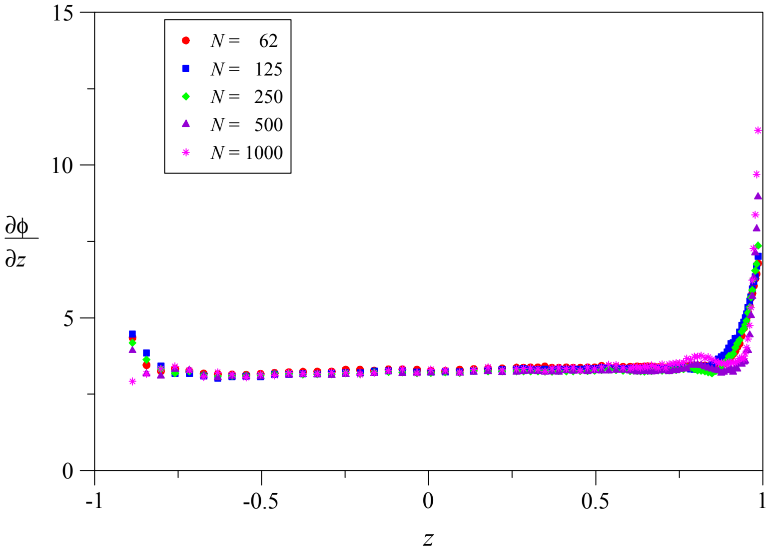

Figure 34: Velocity $u\,(z) \approx \partial\phi/\partial z$ at $x = -5.6$, $y = 0$ for $Ha = 1000$ and different N.

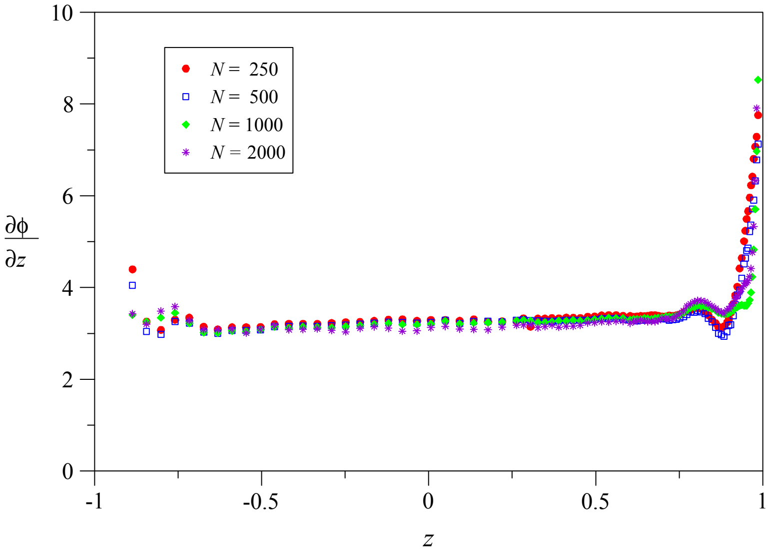

Figure 35: Velocity $u\,(z) \approx \partial\phi/\partial z$ at $x = -5.6$, $y = 0$ for $Ha = 2000$ and different N.

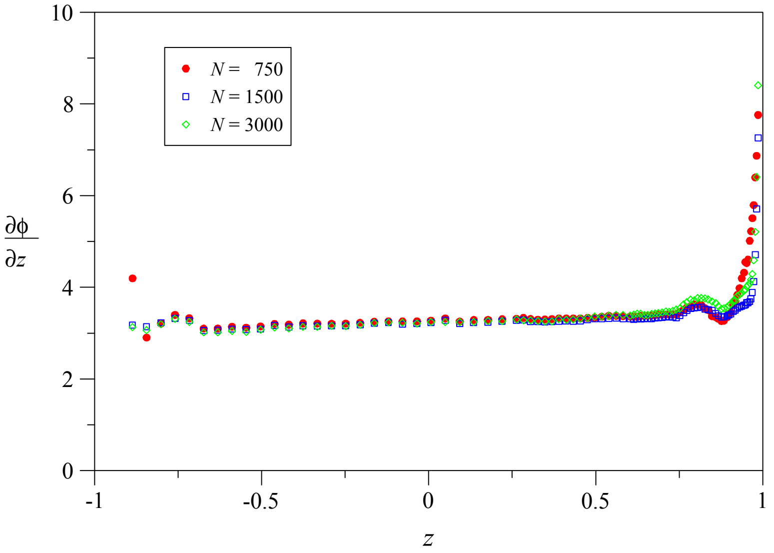

Figure 36: Velocity $u(z) \approx \partial\phi/\partial z$ at $x = -5.6$, $y = 0$ for $Ha = 3000$ and different N.

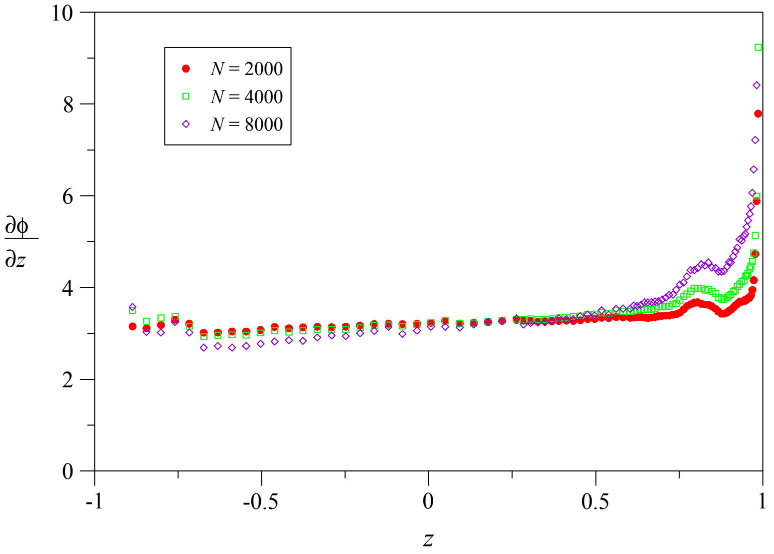

Figure 37: Velocity $u(z) \approx \partial\phi/\partial z$ at $x = -5.6$, $y = 0$ for $Ha = 4000$ and different N.

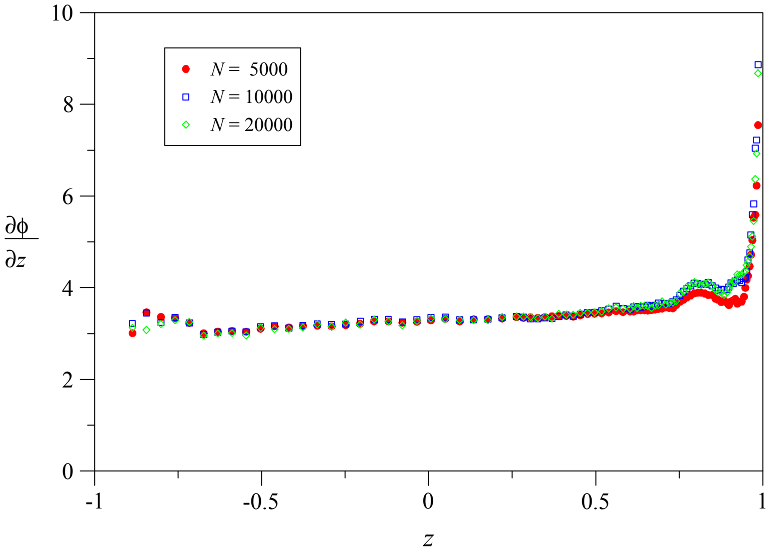

Figure 38: Velocity $u(z) \approx \partial\phi/\partial z$ at $x = -5.6$, $y = 0$ for $Ha = 5000$ and different N.

5.2.3 Profiles of axial velocity at the expansion

When approaching the expansion, the initially flat core velocity profile becomes deformed. Figures 39-41 display this behavior at the expansion at $x = 0$. At this position a thin internal parallel layer is formed along the expansion wall and it spreads along magnetic field lines through the whole cross section. Such layers have been identified e.g. by Hunt and Leibovich (1967) and they are also known as the Ludford layers. For our special geometry we denote the internal layer as expansion layer. These internal layers may be very thin depending on velocity and magnetic field. For creeping flows their thickness scales as $\delta_e \sim Ha^{-1/2}$ or for inertial flows $\delta_e \sim N^{-1/3}$.

The transverse potential gradients shown through Figs. 39-41 are a good indication of axial velocities in the horizontal symmetry plane $y = 0$ of the expansion layer. However, one has to keep in mind that 3D currents at this position are not negligibly small so that $\partial\phi/\partial z$ may differ by a certain amount from the axial velocity u at $x = 0$. This point will be addressed in more details in a separate report. Compared with the upstream flow distribution shown in the previous section the velocity at $x = 0$ is reduced in the center and increased closer to the sides. What appears here as relatively thick side layers is just a result of the deformed velocity profiles in the upstream and downstream cores that are matched through the expansion layer.

Let us consider for the moment the flow at a constant magnetic field e.g. for $Ha = 1000$ as shown in Fig. 39. With increasing the interaction parameter N (decreasing Re) the velocity at the expansion in the center of the duct is slightly reduced up to $N = 2000$ while it again increases by a small amount for $N = 4000$. Simultaneously the side layers become progressively thinner and the maximum velocity in the layers increases. For the investigated interaction parameters one can observe a clear dependence of the side layer velocity on N, while the dependence of the velocity in the core is not so evident. At this Hartmann number the measured potential gradient (indication of the velocity) in the side layer, measured at the smallest possible distance to the wall, exceeds the mean velocity v_0 in the large duct by a factor of 16. All these observations are in accordance with the common understanding of 3D MHD flows, where the 3D extra currents brake the flow in front of the expansion and favour an intense exchange of flow with the side layers.

For stronger magnetic fields, with increasing Hartmann numbers, the side layers become thinner and the influence of inertia effects is not so strongly expressed any more, at least in the investigated range of interaction parameters shown in Fig. 40 for $Ha = 2000$.

By further increasing the Hartmann number to a value of $Ha = 4000$ the side layers become more thinner and the profile of axial velocity in the center of the duct becomes more uniform. Associated with that fact, the velocity in the layer close to the wall should increase further. Unfortunately the maximum of the jet velocity is located so close to the side walls that the peak can not be resolved with the present probe of finite dimension. What can be observed from Fig. 41 is that the side layers depend not so strongly on inertia as for $Ha = 1000$. In the center of the duct, however, some inertial influence remains for $1000 \leq N \leq 4000$. ∫n this range of N the velocity in the center reduces with increasing N. For $N \geq 16000$ inertia seems not to play a significant role any more.

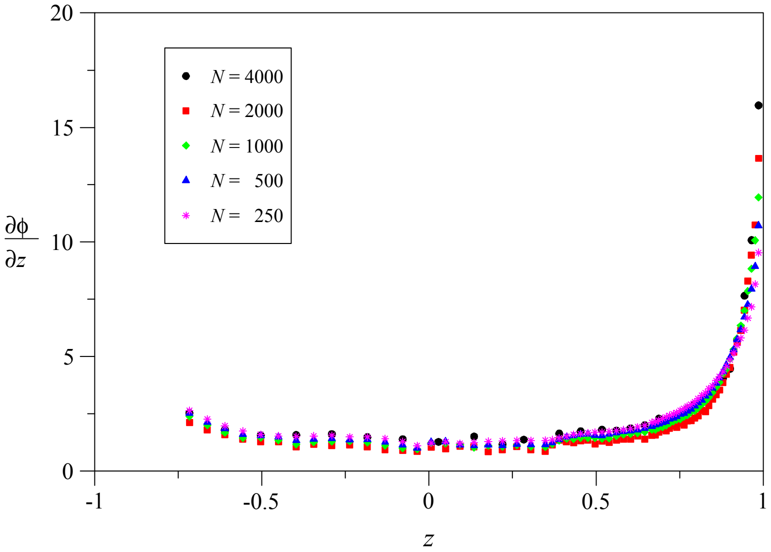

Figure 39: Profiles of transverse potential gradient $\partial\phi/\partial z$ (indication of axial velocity) at $x = 0$ for $Ha = 1000$ and different N

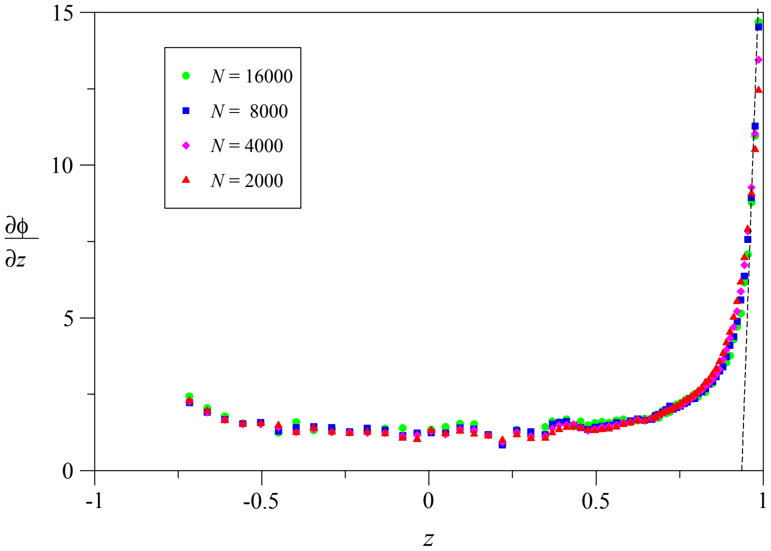

Figure 40: Profiles of transverse potential gradient $\partial\phi/\partial z$ (indication of axial velocity) at $x = 0$ for $Ha = 2000$ and different N

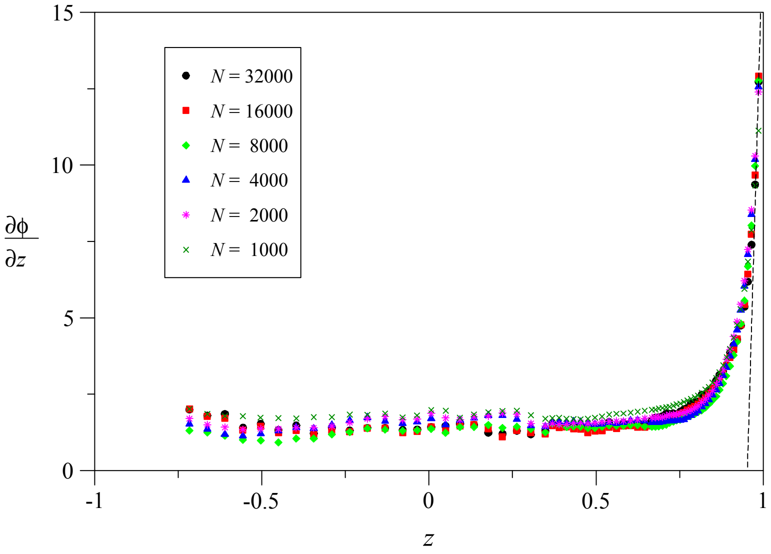

Figure 41: Profiles of transverse potential gradient $\partial\phi/\partial z$ (indication of axial velocity) at $x = 0$ for $Ha = 4000$ and different N

5.2.4 Profiles of transverse velocity at the expansion

So far we investigated the behavior of the axial velocity component u at $x = 0$ in the expansion layer. With the potential probe as shown in Fig. 28, however, it is possible to investigate in addition the flow component w transverse to the main flow direction. Information about the transverse flow may be derived from the negative axial component of potential gradient $-\partial\phi/\partial x$ that gives an indication of the transverse velocity w. Due to the geometry of the probe the axial position at which the transverse velocity is measured is slightly shifted downstream with respect to the expansion and corresponds approximately to the nondimensional position $x \approx 0.01$. As predicted by the asymptotic theory (Bühler (2003)) and as confirmed by numerical analysis (Mistrangelo (2005)) the expansion layer carries an order one flow rate. Since the layer may be very thin for strong magnetic fields the transverse velocity can reach considerable magnitude.

In Figs. 42-44 the axial component of negative potential gradient $-\partial\phi/\partial x$ (indication of transverse velocity w) is shown for various Hartmann numbers and interaction parameters. As expected according to theoretical predictions, high transverse velocities are found already for $Ha = 1000$. We observe here that $w < 0$ for $z < 0$ and $w > 0$ for $z > 0$ which is reasonable since the expansion layer collects a large fraction of the incoming core flow of the small duct and transfers it in a symmetric manner towards the the right and left side layers. This leads to an approximately linear behavior of w near the center. Closer to the sides the input from the upstream core rises, which leads now to a much stronger increase in transverse velocity than in the center of the duct. The highest values of w are observed close to the side walls.

With increasing the interaction parameter the maximum velocity component w increases. The maximum transverse velocity w depends clearly on the interaction parameter and reaches, for the considered range of N, values up to $w \approx 4$ which is already four times larger than the mean velocity v_0. For the highest N (the smallest Re), for which it was possible to obtain reliable data, the flow in the expansion layer is still inertial since w depends essentially on N. Moreover, it's not even possible to estimate or predict the existence of an asymptotic limit for the maximum value of w as $N \rightarrow \infty$.

For higher Hartmann numbers e.g. $Ha = 2000$ or 4000 the maximum axial potential gradient (transverse velocity) in the expansion layer increases further and exceeds even values which are more than 13 times larger than the mean flow v_0 (see Figs. 43, 44).

In order to quantify our observations, let us consider the negative axial potential gradient (transverse velocity w) at a position $z = 0.9$ near the side wall and collect all results for different Ha and N in a single diagram as shown in Fig. 45. The values shown by the filled symbols have been directly taken from the velocity data shown in Figs. 42-44, while the values of the open symbols are estimated from the data according to the local linear fits that are indicated in the figures. One can observe that the magnitude of the axial potential gradient (transverse velocity) increases monotonically with increasing N and it seems the Hartmann number does not play an important role here in the range of investigated parameters. It appears as if the data vary as $N^{0.25}$ for $N < 5000$ (dashed line) while a variation proportional to $N^{0.37}$ (solid line) seems to approximate better the experimental data for $N > 5000$. The most important result here is that even for the highest interaction parameter of $N = 64000$ the flow in the expansion layer remains inertial. Indeed, inertia effects are expected to become negligible according to

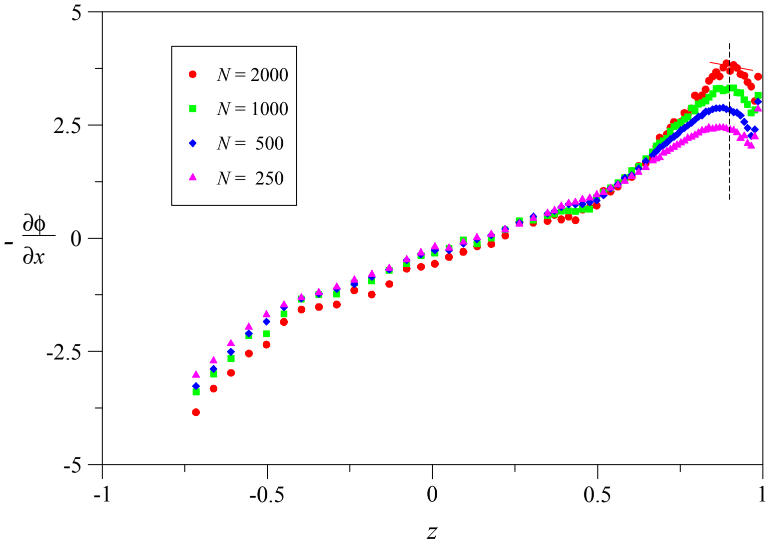

Figure 42: Profiles of negative axial potential gradient $-\partial\phi/\partial x$ (indication of transverse velocity w) at $x \approx 0.01$ for $Ha = 1000$ and different N.

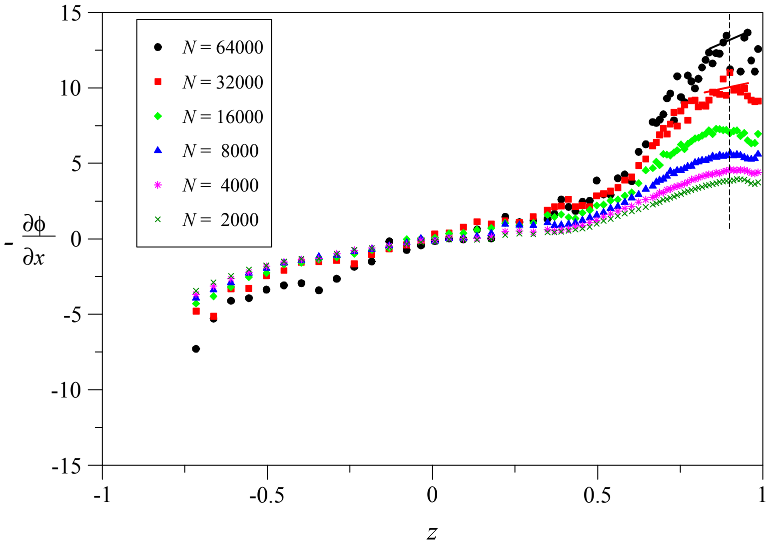

Figure 43: Profiles of negative axial potential gradient $-\partial\phi/\partial x$ (indication of transverse velocity w) at $x \approx 0.01$ for $Ha = 2000$ and different N.

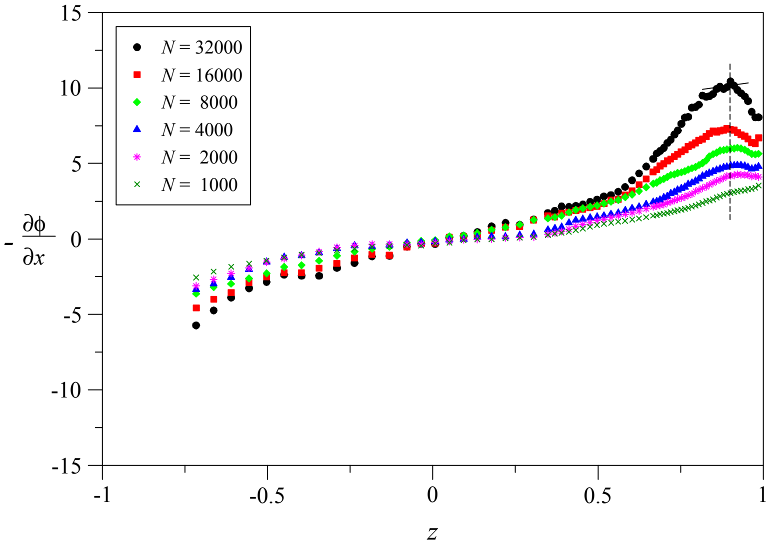

Figure 44: Profiles of negative axial potential gradient $-\partial\phi/\partial x$ (indication of transverse velocity w) at $x \approx 0.01$ for $Ha = 4000$ and different N.

order of magnitude arguments discussed e.g. by Hunt and Leibovich (1967) or Bühler (2003) only if $N \gg Ha^{3/2}$, which is not the case for any of our measurements. For that reason the balance of forces in the layer remains here electromagnetic - inertial with the consequence that the layer thickness, its electric conductance, and the ability to carry mass flux is purely determined by N, independent of the Hartmann number Ha.

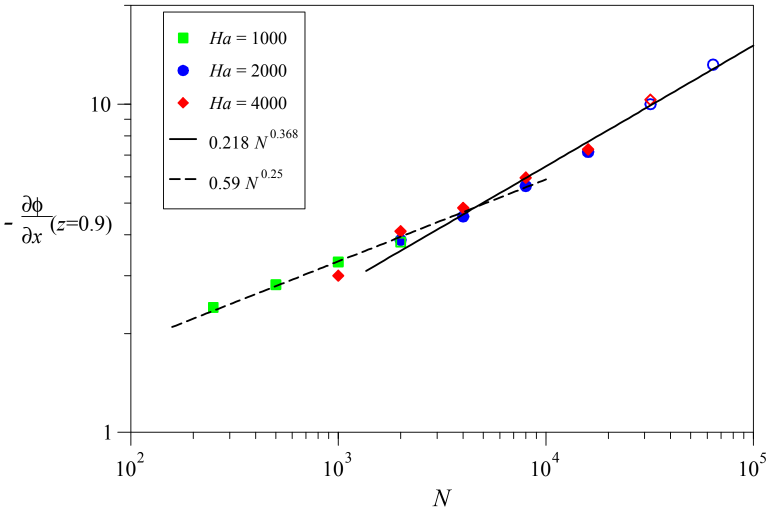

Figure 45: Value of negative axial potential gradient $-\partial\phi/\partial x$ (indication of transverse velocity w) at $x \approx 0.01$, $y = 0$, $z = 0.9$ as a function of N for different values of *Ha*.

5.2.5 Profiles of downstream axial velocity

In the following we consider the axial velocity profiles at the position $x = 1.91$ downstream of the expansion. This position is located not too far from the expansion so that inertia effects, caused by the strong 3D redistribution of the flow at the expansion, are still visible at least for the cases where the Reynolds numbers are high or the interaction parameters are moderate. The influence of inertia can be observed e.g. for the Hartmann number $Ha = 1000$ in Fig. 46. In this figure we observe relatively small core velocities u_{core}, which vary between $0.25 < u_{\text{core}} < 0.5$ and as a result, depending on the interaction parameter, most of the flow is then carried by two jets along the side walls. The lower values for u_{core} are found mainly in the range of moderate N since for these parameters the inertial side layers are quite thick so that they are able to carry a larger amount of flow rate. The flow rate carried by the layers is here close to $Q_s \approx 0.75$. With increasing N the side layers become progressively thinner and approach an asymptotic thickness for $N \geq 1000$ as indicated by the fact that the near wall layers close to $z = 1$ do not differ significantly for $N = 1000$ and $N = 2000$. While the layers become thinner, the maximum velocity in the layers increases so that the flow rate carried by the side layers remains close to $Q_s = 0.5$, i.e. roughly half of the flow is still carried by the layers even for the highest N investigated. The velocity signals for u for $N = 500$ showed a very large scattering so that they can not be exploited here. The reason for that reproducible behavior remains unclear since both the results for $N \leq 250$ and for $N \geq 1000$ behave much better. One possible reason could be an instability that occurs just close to $N = 500$.

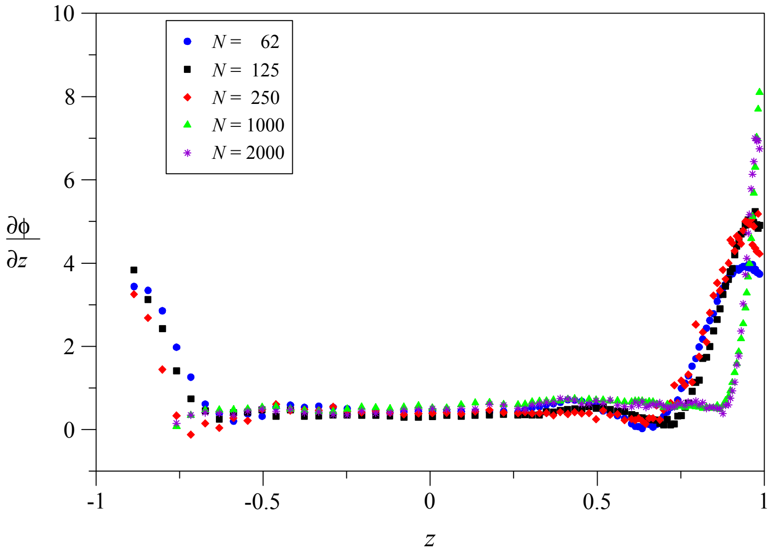

Figure 46: Velocity $u(z) \approx \partial\phi/\partial z$ at $x = 1.91$ for $Ha = 1000$ and different N.

For $Ha = 2000$ one can observe the above described tendency, i.e. the fact that with increasing N the thickness of the side layers becomes smaller. This situation is shown in Fig. 47. At the transition between the side layers and the core a weak reversed flow can be detected. This latter is even more pronounced for the higher Hartmann number of $Ha = 4000$ as shown in Fig. 48. The thickness of the side layers in the inertialess limit as $N \gg 1$ reduces with the Hartmann number as can be seen by a comparison of Figs. 46-48.

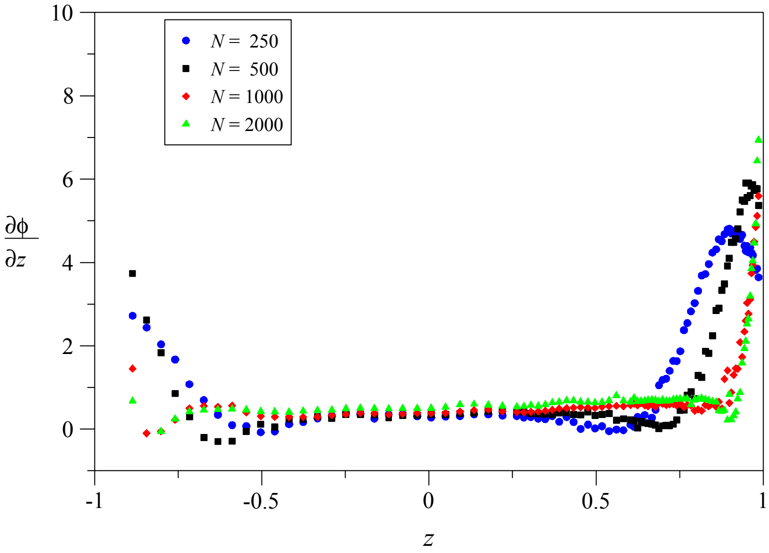

Figure 47: Velocity $u\,(z) \approx \partial\phi/\partial z$ at $x = 1.91$ for $Ha = 2000$ and different N.

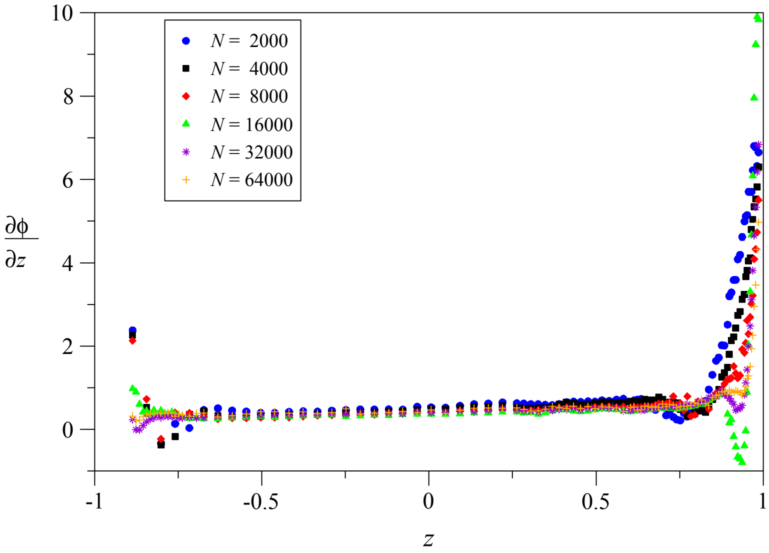

Figure 48: Velocity $u(z) \approx \partial\phi/\partial z$ at $x = 1.91$ for $Ha = 4000$ and different N.

5.3 Surface potential

The instrumentation for measurement of surface potential has been described already in Sect. 4.5. In the following, precise measurements of electric potential on one half of the duct surface i.e. for $z > 0$ are supplemented *and* shown for the entire geometry by assuming symmetry with respect to the vertical plane $z = 0$. The assumption of symmetry has been checked by comparison of two surface potential values on the other half of the duct for $z < 0$, for each cross section. The measured physical potential values have been scaled by the reference potential $\phi_0 = Lv_0B_0$ and plotted in Figs. 49-70 shown below. The results of all measurements can be shortly summarized as follows.

In the small duct the velocity is four times higher than in the large duct. For that reason the induced transverse potential gradient in the small duct is higher than that in the large one. Far upstream the flow is fully established. This can be seen by isolines of potential that are perfectly aligned with the flow. When the flow approaches the expansion the transverse potential gradient is reduced and one can observe the 3D distortion of the flow in the vicinity of the expansion on the Hartmann walls and preferentially at the side walls. Further downstream the flow reaches again fully established conditions where isolines of potential are aligned with the flow. What can be seen from all the figures is that the surface potential represented in the current scaling does not vary too sensitively changing the magnetic fields (Ha) or the flow rates (N).

Since the potential may serve as an approximate streamfunction of the flow, the pictures shown below give a good overall imprecision how the flow redistributes at the expansion. The flow follows mainly lines of constant color. One can observe that at the expansion the flow is pushed towards the side walls from where it is partly redistributed to the core of the large duct. All these observations are in accordance with measurements of local flow quantities and with theoretical predictions.

Results from a first measuring campaign are shown in Fig. 49 for $Ha = 1000$, $N = 1000$. During this campaign potential differences had been measured with reference to a single ground that was connected through a separate cable to the nano-voltmeter. The electric noise that was trapped by the wire loop yielded results that loose their meaning at least behind the expansion, where the signals are very weak. For that reason the wiring was changed in essential parts. In particular the ground was carried through each individual measuring cable and switched also during measurements by a multiplexer. With the new wiring the signal/noise ratio could be improved by far more than an order of magnitude. Results, obtained from a second measuring campaign using the improved wiring, are shown in Fig. 50 for $Ha = 1000$ and $N = 1000$. And they can be compared with the theoretical results based on asymptotic theory displayed in Fig. 51. Inertia effects seem to play not a decisive role for surface potentials since the results for smaller interaction parameters (not explicitly shown here) do practically not differ from the results for $Ha = 1000$ and $N = 1000$. This might have its origin in the fact that 3D inertial currents find their path mainly inside the fluid without influencing too much the wall potential.

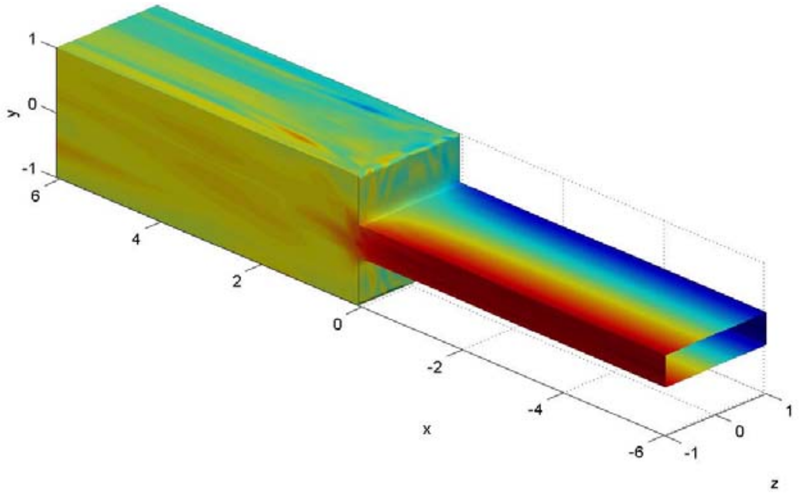

Figure 49: Colored contours of measured surface potential for $Ha = 1000$, $N = 1000$ from an early campaign with insufficient wiring.

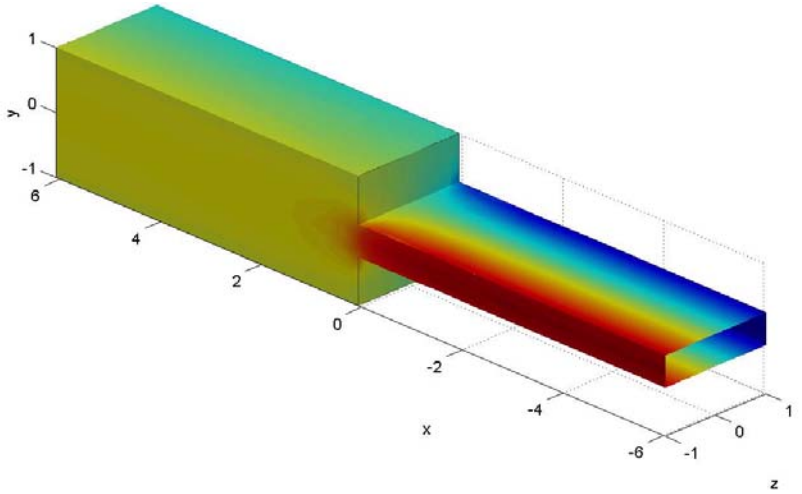

Figure 50: Colored contours of measured surface potential for $Ha = 1000$, $N = 1000$, obtained by using an improved wiring.

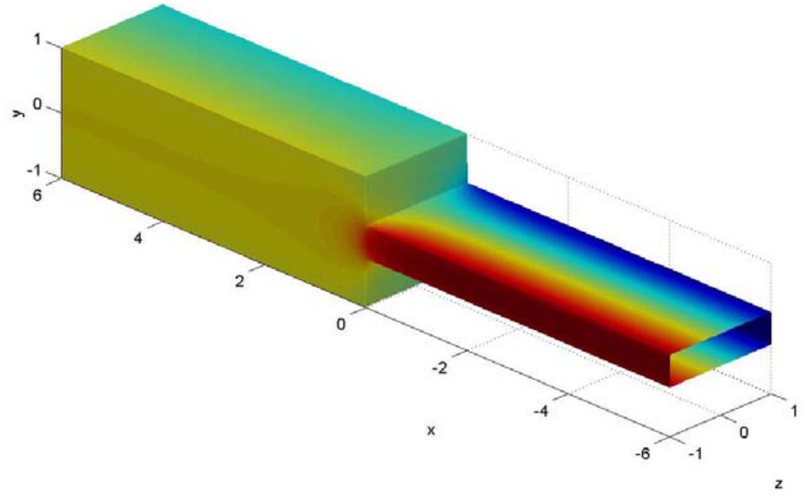

Figure 51: Colored contours of calculated surface potential for $Ha = 1000$, $N = \infty$.

Similar results have been obtained for higher Hartmann numbers. As examples results for $Ha = 2000$ and different values of N are displayed below, starting with $N = 500$ in Fig. 52 up to $N = 4000$ in Fig. 55. A comparison of all investigated surface potential data shows again no significant dependence on the interaction parameter and good agreement with theoretical results (Fig. 56) obtained by the asymptotic theory valid for $N \to \infty$. In order to quantify the results we show in Fig. 57 the potential measured along the side wall in the plane of symmetry, i.e. $\phi\,(x, z = 1, y = 0)$. Most surprising is that inertia effects are confined mainly to the fully developed parts of the flow. Even at the expansion, where inertia effects are expected to be most significant the behavior of surface potential is not affected. It can be observed that the measured potentials both in the small and in the large duct are slightly below the line that has been obtained from asymptotic theory. With increasing N the measured potentials, however seem to converge towards the asymptotic results, which are valid as $N \to \infty$. Theoretically the fully developed flow near the entrance or the exit should not depend on N. One reason for the observed behavior could be the fact that at a certain critical Reynolds number the side layers tend to become unstable. A higher momentum transfer with the core then leads to decreased velocities in the jets with the consequence that the potential maximum at the sides is reduced. But this point needs further investigation.

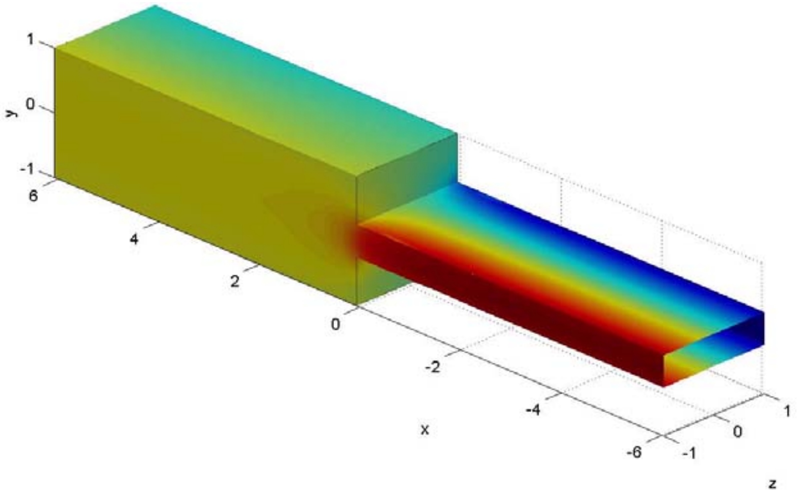

Figure 52: Colored contours of measured surface potential for $Ha = 2000$, $N = 500$.

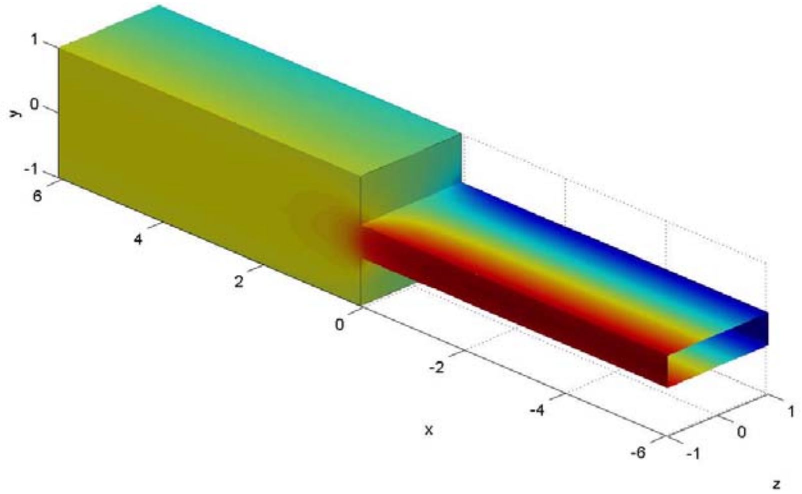

Figure 53: Colored contours of measured surface potential for $Ha = 2000$, $N = 1000$.

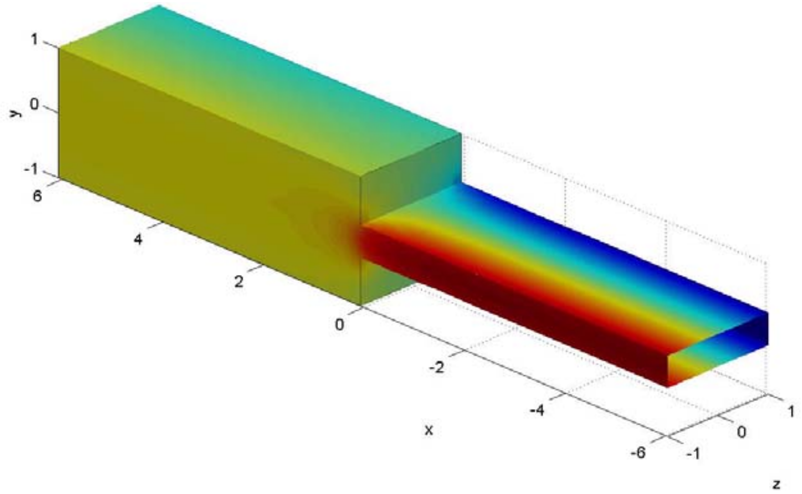

Figure 54: Colored contours of measured surface potential for $Ha = 2000$, $N = 2000$.

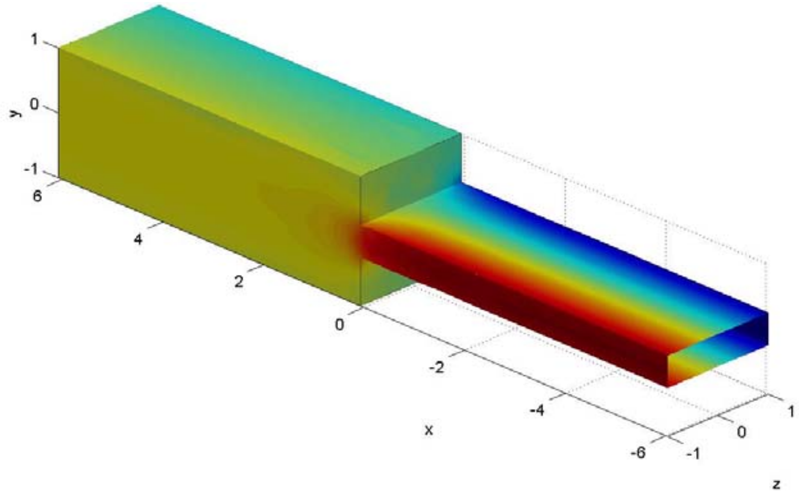

Figure 55: Colored contours of measured surface potential for $Ha = 2000$, $N = 4000$.

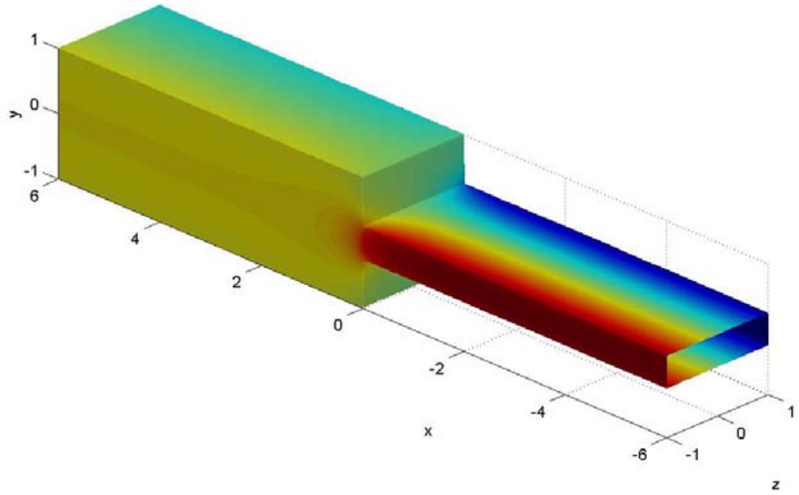

Figure 56: Colored contours of calculated surface potential for $Ha = 2000$, $N = \infty$.

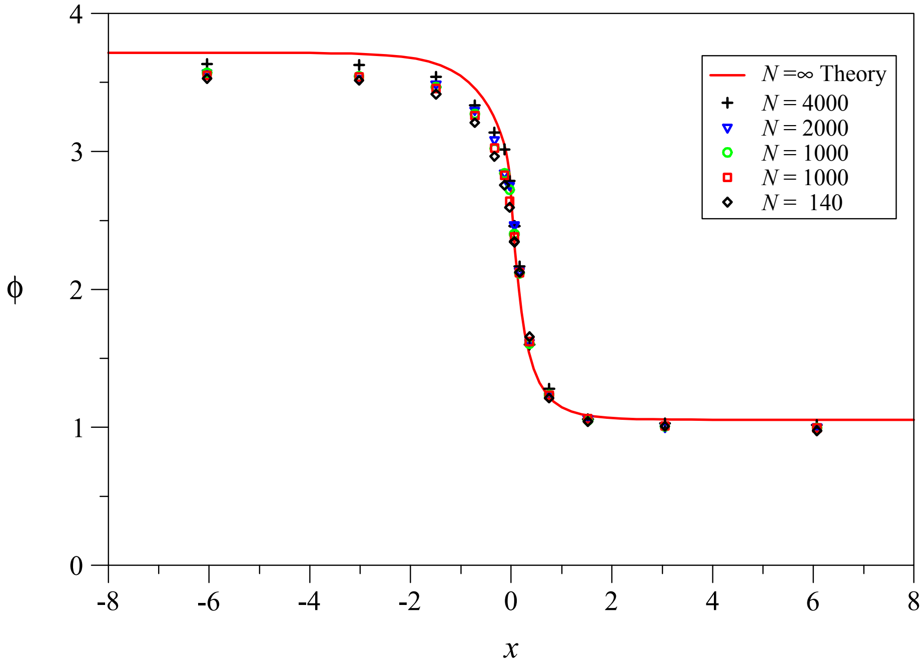

Figure 57: Side wall potential in the plane of symmetry, $\phi\,(x, y = 0, z = 1)$, along the axial coordinate x for $Ha = 2000$.

For higher Hartmann numbers the situation is analogous, i.e. the inertial influence of the expansion on side wall potential seems to be not too significant. Results for the Hartmann number of $Ha = 3000$ are displayed through Figs. 58-62. A comparison of the results obtained at the highest interaction parameter $N = 6000$, shown in Fig. 62, with the results of the asymptotic theory, displayed in Fig. 63, shows quite good agreement. This indicates once again that inertia effects on side wall potential are negligible already for $N \geq 6000$. The results are displayed quantitatively in Fig. 64, in which the side wall potential $\phi(x, y = 0, z = 1)$ is plotted along the axial coordinate x. The most pronounced effect of inertia is here (as for $Ha = 2000$) observed rather for the flow in the entrance pipe than for the expansion region. This behavior could be caused again by unstable flows in the side layers of the small pipe. At higher N those layers stabilize and the potential values converge to the predicted asymptotic solution.

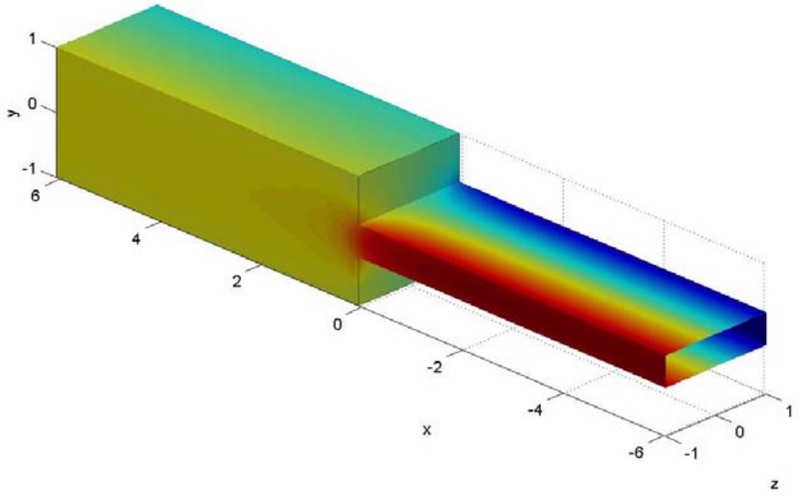

Figure 58: Colored contours of measured surface potential for $Ha = 3000$, $N = 400$.

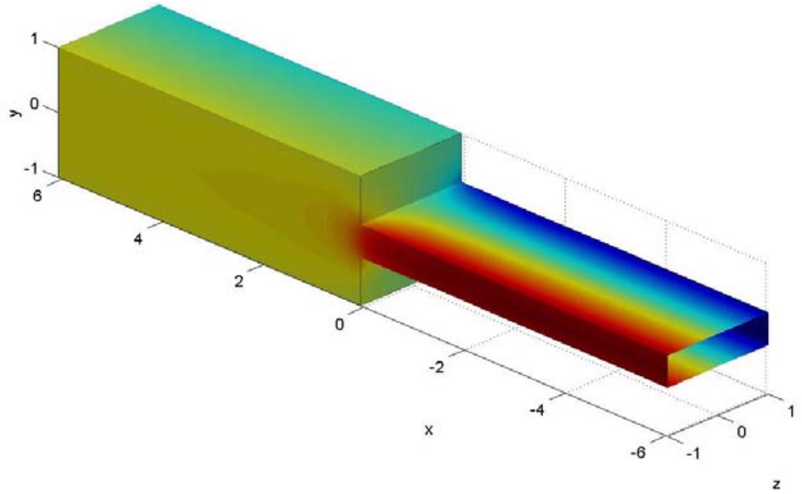

Figure 59: Colored contours of measured surface potential for $Ha = 3000$, $N = 750$.

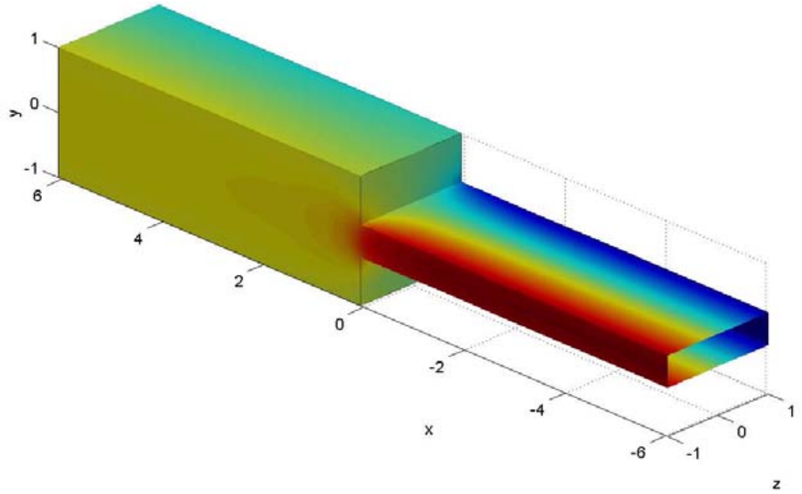

Figure 60: Colored contours of measured surface potential for $Ha = 3000$, $N = 1500$.

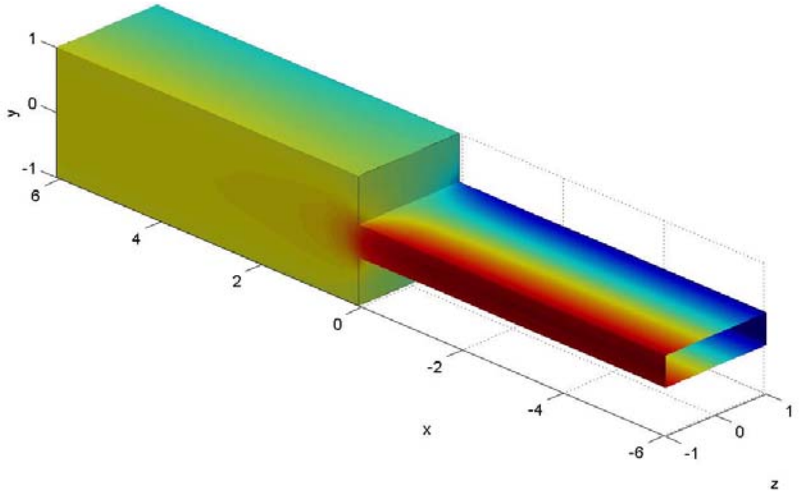

Figure 61: Colored contours of measured surface potential for $Ha = 3000$, $N = 3000$.

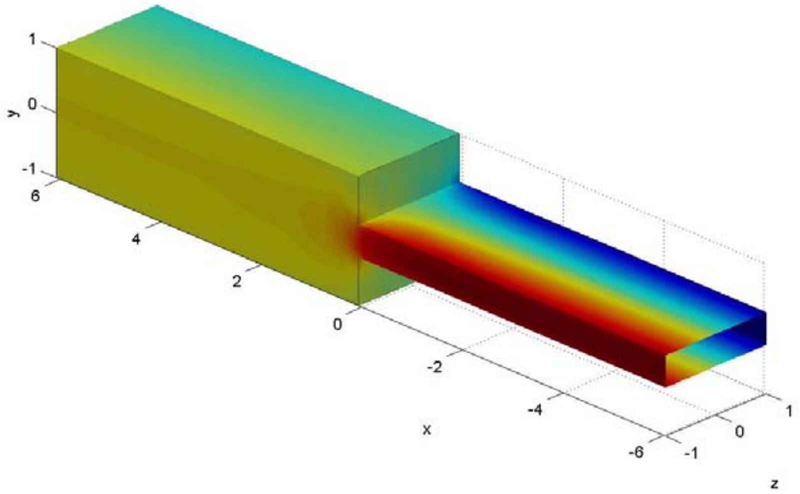

Figure 62: Colored contours of measured surface potential for $Ha = 3000$, $N = 6000$.

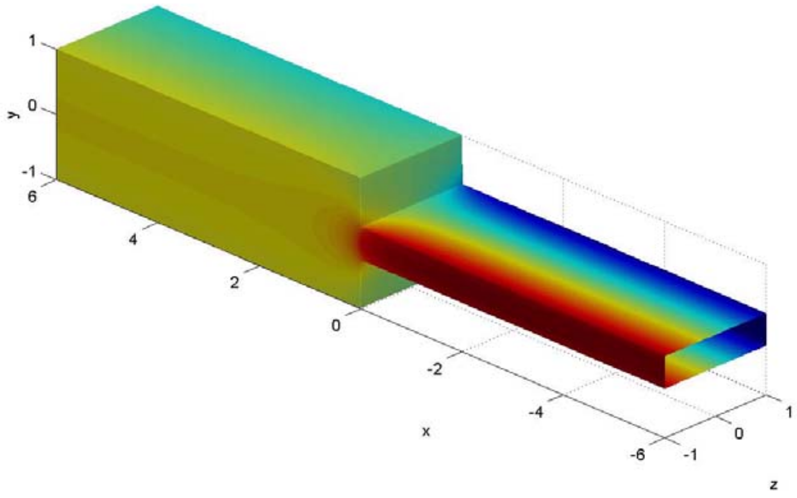

Figure 63: Colored contours of calculated surface potential for $Ha = 3000$, $N = \infty$.

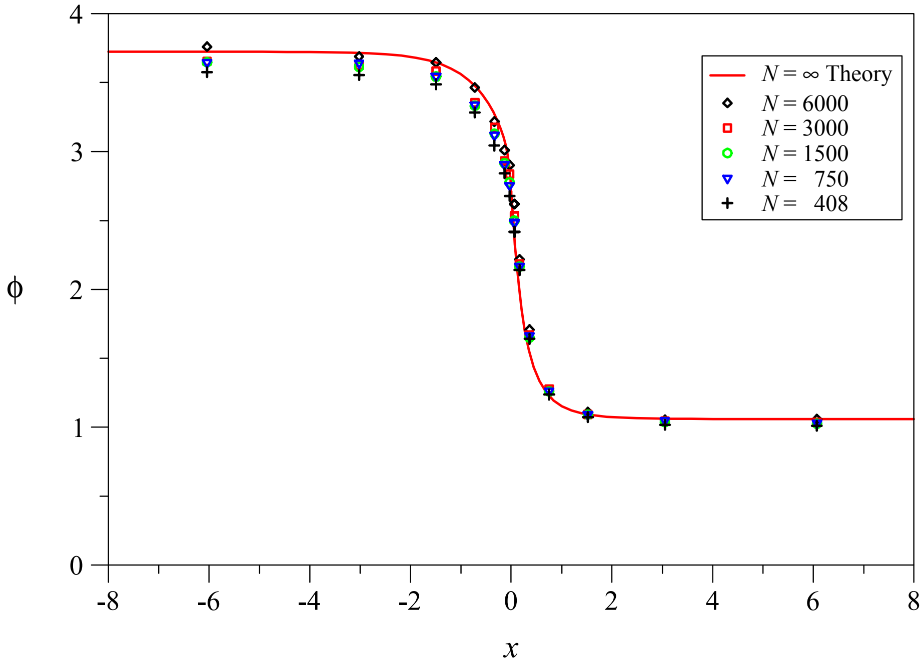

Figure 64: Side wall potential in the plane of symmetry, $\phi\left(x, y = 0, z = 1\right)$, along the axial coordinate x for $Ha = 3000$.

All the behavior explained above is still present if the Hartmann number is progressively increased. Finally we display qualitative results for $Ha = 5000$ through Figs. 65-69 and quantitative comparison in Fig. 70. The agreement both qualitatively and quantitatively with the asymptotic results becomes even better with increasing the Hartmann number. There could be two reasons for that. One is that side layers remain stable over a wider range of N. The other explanation could be that, once the layer is unstable, the perturbations remain within the layer that becomes thinner and thinner with increasing Ha so that the influence on the global behavior, expressed through the surface potential, is negligible. For $Ha = 5000$ the inertial influence on side wall potential is practically not important.

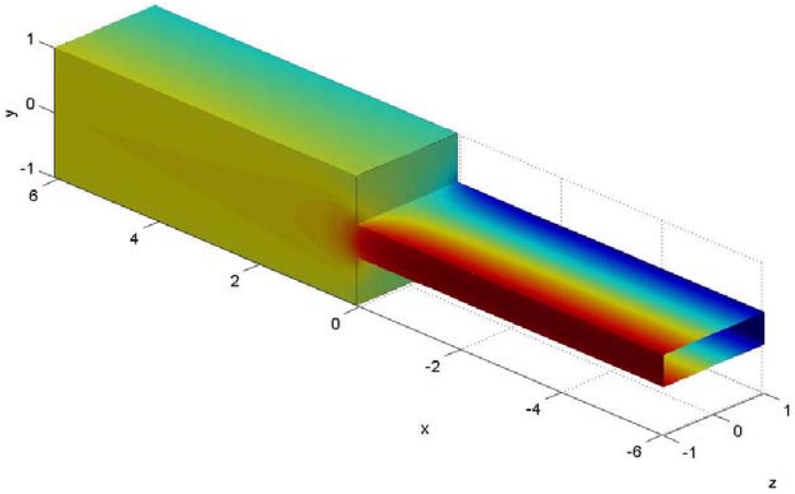

Figure 65: Colored contours of measured surface potential for $Ha = 5000$, $N = 2500$.

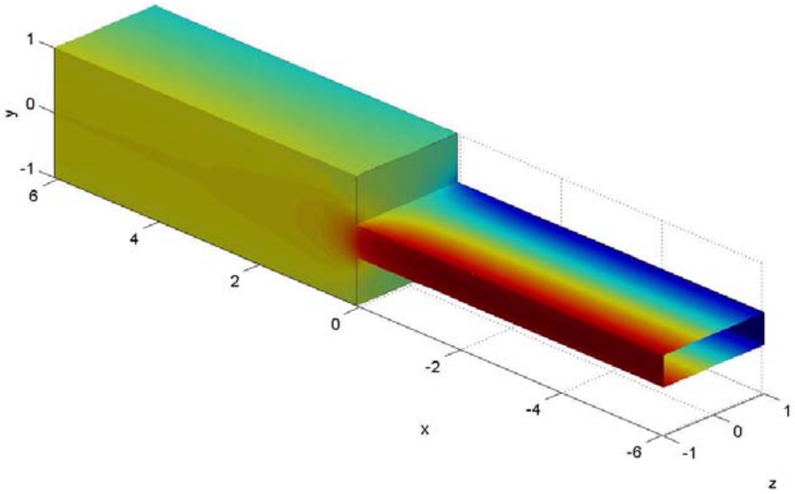

Figure 66: Colored contours of measured surface potential for $Ha = 5000$, $N = 5000$.

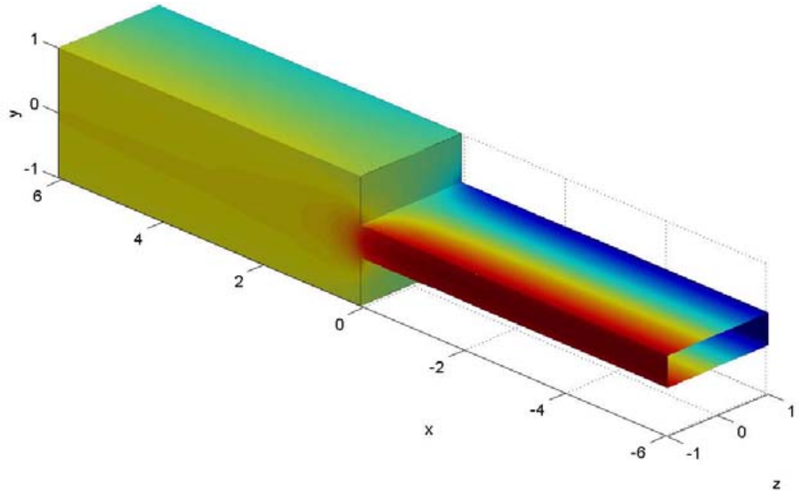

Figure 67: Colored contours of measured surface potential for $Ha = 5000$, $N = 10000$.

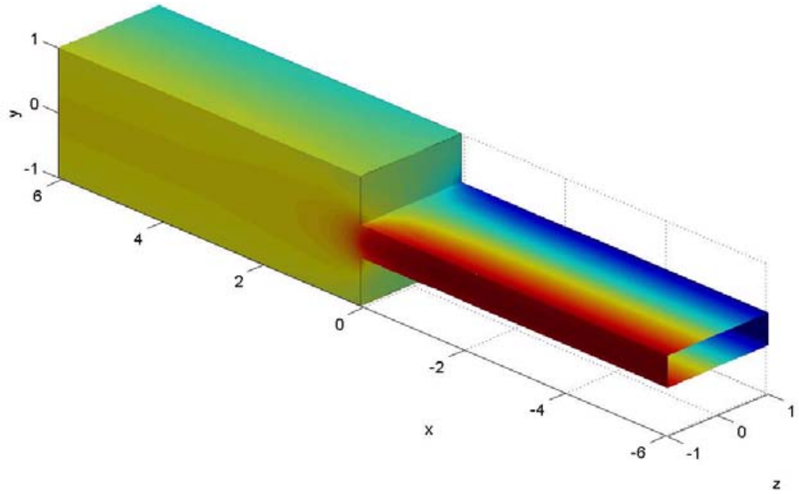

Figure 68: Colored contours of measured surface potential for $Ha = 5000$, $N = 20000$.

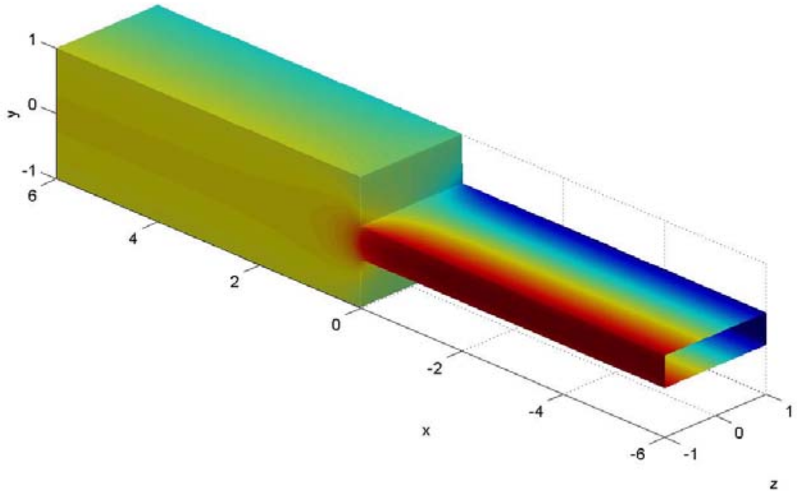

Figure 69: Colored contours of calculated surface potential for $Ha = 5000$, $N = \infty$.

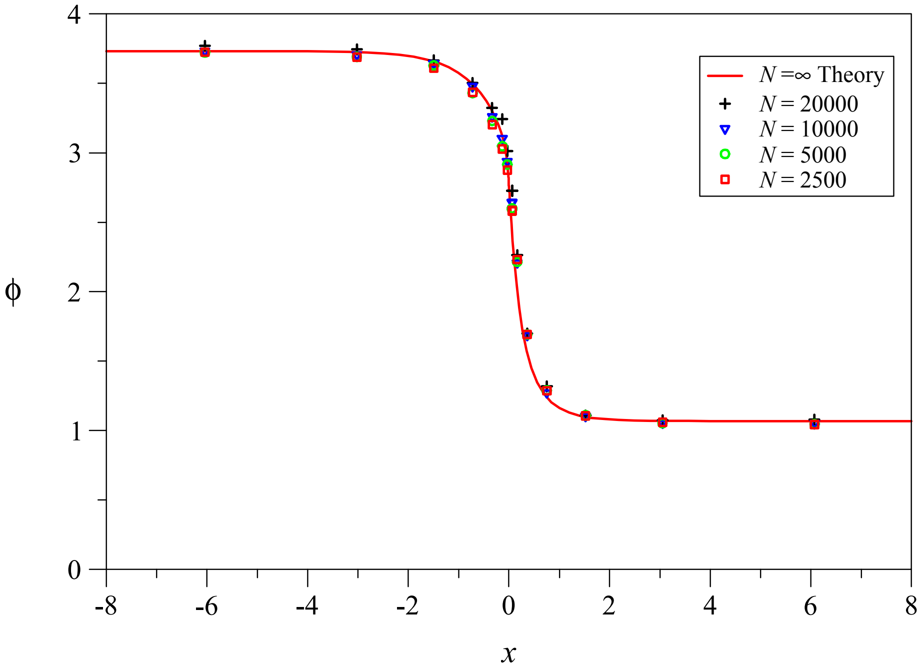

Figure 70: Side wall potential in the plane of symmetry, $\phi(x, y = 0, z = 1)$, along the axial coordinate x for $Ha = 5000$.

6 Conclusions

Three dimensional liquid-metal MHD flows in a plane sudden expansion (along magnetic field lines) of rectangular ducts have been investigated experimentally in the MEKKA laboratory of the Forschungszentrum Karlsruhe. The experiments were performed in strong magnetic fields that allow to reach high Hartmann numbers and interaction parameters, approaching the fusion relevant parameter range. In the experiments Hartmann numbers Ha of more than 5000 and interaction parameters N as high as $N = 130\,000$ could be achieved. For such values of parameters the fluid behaves as being inviscid and nearly inertialess in the so-called cores that occupy most of the fluid volume. Viscous (and inertial) effects are confined within thin boundary or internal layers.

The flow was investigated through measurements of pressure variation along the upper Hartmann wall, by measuring surface potential on the duct walls and by local potential gradient probes, which were travelled through the channel width at several cross sections.

Measurements of pressure gradients and gradients of surface potential both far upstream and downstream of the expansion showed that the test section was long enough that fully developed flow conditions are well established before the flow reaches the expansion, i.e. $\partial^2 p/\partial x^2 = 0$ and $\partial\phi/\partial x = 0$. Moreover, gradients of pressure upstream and downstream the expansion coincide quite well with those predicted by an asymptotic analysis. This fact is a good indication that the fluid is perfectly wetting the walls, i.e. that contact resistance is negligible. These conditions are necessary requirements for a comparison with results obtained by theoretical tools.

When approaching the expansion the pressure drops more rapidly due to extra Lorentz forces opposing the flow, caused by additional electric current loops present at the expansion. Behind the expansion the pressure gradient is reversed, i.e. part of the pressure drop is recovered by the action of Lorentz forces acting now in flow direction. All these phenomena have been observed experimentally for Hartmann numbers in the range of $500 \leq Ha \leq 5000$.

The influence of inertia on pressure drop has been studied by varying the interaction parameter N over a wide range $33 < N < 130\,000$. The measurements indicate clearly that the expansion causes an additional fraction of pressure drop Δp_{3D} due to three-dimensional effects near the expansion. It has been shown that the influence of inertia and viscous effects can be summarized by a correlation of the type

$$\Delta p_{3D} = 0.315 + 4.76\, Ha^{-1/2} + (8.2 \pm 2.2) \cdot 10^{-3}\, Re^{1/3}, \tag{26}$$

where the Reynolds number has been defined as $Re = Ha^2/N$. This additional 3D pressure drop consists of three parts. The first part is present even for inviscid and inertialess ($N = \infty$) flows and depends on the geometry and wall conductivity. The second term accounts for viscous effects and the third term represents the inertial influence. One should note here, that the first two terms which have been obtained by an asymptotic numeric approach, fit quite well into the experimental data base. It has been shown, depending on the governing parameters, that viscous and inertia effects may contribute significantly to the 3D pressure drop Δp_{3D}.

A comparison of the measured pressure values with results from an asymptotic theory valid for $N \to \infty$, shows quite good agreement in the sense that experimentally obtained data points converge monotonically towards the theoretical values as N is increased. For the highest values of N that could be realized experimentally, however, one can still find some weak inertial influence. This indicates that even the highest values of N, which could be realized in the experiment, were not large enough that the flow was perfectly inertialess. For small values of N inertia may double the 3D pressure drop Δp_{3D} in comparison with that of an inertialess flow.

Measurements of surface potential have been performed using an array of more than 300 potential probes, distributed with higher density near the expansion. A qualitative and quantitative comparison with the asymptotic theory shows also quite good agreement. All theoretically predicted features could be observed in the experiment. Since the potential may serve as a hydrodynamic streamfunction for the fluid flow inside the duct, the isolines of potential obtained from the experimental data give already a comprehensive picture of the redistribution of the flow at the expansion. Approaching the expansion the flow, which was initially carried by the core in the smaller duct, is driven toward the sides. Part of that flow enters the upstream side layers in front of the expansion but another part enters also the large cross section directly. This part is collected by an internal layer from where it is redistributed mainly towards the sides. Further downstream a certain amount is redistributed to the core flow in the large duct. The quantitative comparison of side wall potential with theoretically predicted results is in good agreement for large N. Surprising is here the fact that the side wall potential in the fully developed upstream region depends clearly on N but seems to converges to the asymptotic results as $N \to \infty$. This fact may has its origin perhaps in the occurrence of instabilities of the upstream side layer jets at lower values of N (higher Re). Those instabilities have been detected also by local probes placed inside the flow. With increasing N (decreasing Re) the amplitude of the perturbations decays and the flow approaches laminar condition in agreement with the inertialess theory. This point will be further analyzed in a separate report. With increasing Hartmann number the instabilities exert stronger damping, they are confined to thinner layers, and their inertial influence on the upstream side layer potential becomes weaker. At the expansion some small effects of inertia on the side layer potential remains.

Using traversable probes at the expansion it was possible to determine the local transverse potential gradient $\partial\phi/\partial z$, which is an indication of the local axial velocity component u. As expected from theoretical analyses the flow in the center of the duct gets depressed and the magnitude of the potential gradient (velocity) near the sides is increased compared to the upstream values. Maximum velocities of more than 15 were detected. For a given Hartmann number of $Ha = 1000$ one can identify the influence of inertia by a decrease of the center values of $\partial\phi/\partial z$ as N is increased. Simultaneously the inertial side layer becomes thinner and the velocity close to the side wall increases. For $Ha = 2000$ the side layer becomes thinner but the inertial influence is not so strongly expressed for the considered values on N. For $Ha = 4000$ the side layer thickness decreases further and the core becomes more flat. The side layers seem not to depend strongly on N whereas a weak inertial influence on the velocities in the center is observed for $N < 4000$.

Inspection of the local axial potential gradients $-\partial\phi/\partial x\,(z = 0.9)$ (indication of transverse velocity $w\,(z = 0.9)$) near the side wall yields at the expansion a typical behavior as $-\partial\phi/\partial x \sim N^{0.25}$ for $N < 5000$ and $\sim N^{0.37}$ for $N > 5000$ with maximum values of more than 12 for the highest values of $N = 64000$. These results indicate explicitly that the internal layer remains inertial for all values of N investigated here.

The discussed experimental results obtained for a plane sudden expansion at high Hartmann numbers and interaction parameters extend the current data base for 3D MHD flows. The present experiment is of fundamental interest not only for applications in fusion but it may serve also as a basis for validation of existing and upcoming computational tools.

References

Barleon, L., Mack, K.-J. and Stieglitz, R.: 1996, The MEKKA-facility - a flexible tool to investigate MHD-flow phenomena, *Report FZKA 5821*, Forschungszentrum Karlsruhe.

Branover, G. G., Vasil'ev, A. S. and Gel'fgat, Y. M.: 1967, Effect of a transverse magnetic field on the flow in a duct at a sudden cross section enlargement, *Magnitnaya Gidrodynamica* **3**(3), 61–65.

Bühler, L.: 2003, Inertialess magnetohydrodynamic flow in expansions and contractions, *Report FZKA 6904*, Forschungszentrum Karlsruhe.

Chang, C. and Lundgren, S.: 1961, Duct flow in magnetohydrodynamics, *Zeitschrift für angewandte Mathematik und Physik* **XII**, 100–114.

Gel'fgat, Y. M. and Kit, L. G.: 1971, Investigation of the conditions of occurrence of M-shaped velocity profiles at sudden expansion or contraction of a magnetohydrodynamic flow, *Magnetohydrodynamics* **7**(1), 21–25.

Hunt, J. C. R. and Leibovich, S.: 1967, Magnetohydrodynamic flow in channels of variable cross-section with strong transverse magnetic fields, *Journal of Fluid Mechanics* **28**(Part 2), 241–260.

Jauch, U., Karcher, V., Schulz, B. and Haase, G.: 1986, Thermophysical properties in the system Li-Pb, *Report KfK 4144*, Kernforschungszentrum Karlsruhe.

Mistrangelo, C.: 2005, *Three-dimensional MHD flow in sudden expansions*, PhD thesis, Universität Karlsruhe, FZKA 7201, Forschungszentrum Karlsruhe.

Picologlou, B. F., Reed, C. B., Hua, T. Q., Barleon, L., Kreuzinger, H. and Walker, J. S.: 1989, MHD flow tailoring in first wall coolant channels of self-cooled blankets, *Fusion Engineering and Design* **8**, 297–303.

Stahl-Eisen-Werkstoffblätter: 1992, *Physikalische Eigenschaften von Stählen*, Verein Deutscher Eisenhüttenleute.

Walker, J. S.: 1981, Magnetohydrodynamic flows in rectangular ducts with thin conducting walls, *Journal de Mécanique* **20**(1), 79–112.

Walker, J. S., Ludford, G. S. S. and Hunt, J. C. R.: 1972, Three-dimensional MHD duct flows with strong transverse magnetic fields. Part 3. Variable-area rectangular ducts with insulating walls, *Journal of Fluid Mechanics* **56**, 121–141.

Wetzel, C.: 2004, *Volumenkraftgetriebene magnetohydrodynamische Strömungen*, Master's thesis, Universität Karlsruhe.